Gap Junctional Versus Paracrine Signaling in the Human Lens Epithelium: Analysis Based on Multicellular Ca^{2+} Imaging and Computational Modeling

Marko Šterk,[1–4] Elena Thaler,[5,6] Aleš Fajmut,[2,7] Marko Hawlina,[5] Marko Gosak,[1,2,4] and Sofija Andjelic[5]

[1]Faculty of Medicine, University of Maribor, Maribor, Slovenia
[2]Faculty of Natural Sciences and Mathematics, University of Maribor, Maribor, Slovenia
[3]Institute of Information Science, Maribor, Slovenia
[4]Alma Mater Europaea University, Maribor, Slovenia
[5]Eye Hospital, University Medical Centre, Ljubljana, Slovenia
[6]Institute of Translational Medicine, Faculty of Medical Sciences, Private University in the Principality of Liechtenstein (UFL), Triesen, Liechtenstein
[7]Faculty of Health Sciences, University of Maribor, Maribor, Slovenia

Correspondence: Marko Gosak, Faculty of Medicine, University of Maribor, Maribor 2000, Slovenia; marko.gosak@um.si.
Sofija Andjelic, Eye Hospital, University Medical Centre, Ljubljana 1000, Slovenia; sofija.andjelic@kclj.si.

Received: June 24, 2025
Accepted: October 20, 2025
Published: November 17, 2025

Citation: Šterk M, Thaler E, Fajmut A, Hawlina M, Gosak M, Andjelic S. Gap junctional versus paracrine signaling in the human lens epithelium: Analysis based on multicellular Ca^{2+} imaging and computational modeling. *Invest Ophthalmol Vis Sci.* 2025;66(14):39. https://doi.org/10.1167/iovs.66.14.39

Purpose. Effective intercellular communication among lens epithelial cells (LECs) is essential for lens homeostasis, and its disruption has been implicated in cataract formation. This study investigates the mechanisms of calcium (Ca^{2+}) wave propagation in the human lens epithelium, focusing on the respective roles of gap-junctional coupling and ATP-mediated paracrine signaling.

Methods. We performed multicellular Ca^{2+} imaging on human postoperative anterior lens capsule preparations obtained from cataractous lenses during cataract surgery which retained intact monolayers containing viable LECs. Mechanically induced Ca^{2+} waves were recorded, and the contribution of specific signaling pathways was evaluated by pharmacological intervention using apyrase (an ATP-hydrolyzing enzyme) and carbenoxolone (CBX; a gap-junctional blocker). To interpret the experimental results, we developed a biophysically detailed computational model of the LEC monolayer, incorporating intracellular Ca^{2+} dynamics, gap-junctional IP_3/Ca^{2+} diffusion, and extracellular ATP signaling.

Results. Apyrase moderately reduced the spatial extent, amplitude, and duration of Ca^{2+} waves without affecting propagation speed. In contrast, CBX significantly suppressed wave transmission, limiting activation to cells directly adjacent to the stimulation site. Simulations reproduced key experimental features and indicated that neither pure gap-junctional nor purely paracrine signaling mechanisms alone could explain the observed dynamics. Instead, a hybrid mechanism combining gap-junctional communication and partially regenerative ATP release was required.

Conclusions. Our results highlight the cooperative roles of gap-junctional and ATP-based paracrine signaling in mediating mechanically induced Ca^{2+} wave propagation in the human lens epithelium. This dual-pathway mechanism may be critical for coordinated cellular responses that support physiological processes such as ion homeostasis and transparency maintenance in the human lens.

Keywords: human lens epithelium, calcium signaling, intercellular communication, calcium imaging, computational model

The human lens comprises a monolayer of lens epithelial cells (LECs) overlying concentric layers of fiber cells in the anterior segment of the eye, where it focuses light onto the retina. The epithelial monolayer lies on the anterior surface, beneath the lens capsule (LC), a specialized basement membrane that envelops the entire lens, and above the outermost fiber layer. LECs have typical epithelial morphology and are tightly packed, cuboidal cells measuring approximately 5.5 to 8 µm in height and 7 to 11 µm in width.[1] We previously detailed the structural organization of LECs: the apical side facing the fiber cells is smooth, whereas the basal side in contact with the LC exhibits enlarged membrane extensions and interdigitations.[2] Although the epithelium represents a small fraction of lens mass, organelle-rich LECs are central to lens homeostasis and transparency.[3] Positioned between the aqueous humour and fibers, the epithelium forms a barrier with tight junctions[4] and expresses connexins and transport pathways that mediate intercellu-

lar communication and solute exchange essential for lens function.[3,5,6] Given their pivotal role in maintaining lens physiology, it is not surprising that dysfunction of LECs has been closely linked to the onset and progression of cataracts. Cataract, the loss of lens transparency, remains the leading cause of blindness worldwide.[7,8] Several lines of evidence implicate disruption of Ca^{2+} homeostasis in the lens as an early driver of cataractogenesis.[9–11] Ca^{2+} is a ubiquitous second messenger in lens epithelial signaling. Accordingly, dissecting the processes that regulate Ca^{2+} influx, intracellular storage and buffering, and plasma-membrane extrusion is key to understanding cataractogenesis.

Cytosolic Ca^{2+} homeostasis in human LECs is maintained primarily by the plasma membrane Ca^{2+}-ATPase (PMCA) and the sarcoplasmic/endoplasmic reticulum Ca^{2+}-ATPase (SERCA), which extrude Ca^{2+} across the plasma membrane and sequester Ca^{2+} into the endoplasmic reticulum (ER), respectively, with the Na^+/Ca^{2+} exchanger (NCX) providing a secondary route during elevations of intracellular Ca^{2+} concentration ($[Ca^{2+}]_i$).[12] $[Ca^{2+}]_i$ signals are generated by ER release through inositol 1,4,5-trisphosphate receptors (IP_3Rs) and ryanodine receptors (RyRs), whereas additional influx arises via mechanosensitive and voltage-operated Ca^{2+} channels and via store-operated Ca^{2+} entry.[12–16] Purinergic pathways further couple extracellular nucleotides to IP_3-dependent ER release via P2Y receptors and to rapid cation entry via P2X receptors, providing a mechanistic link to mechanically induced responses.[12,17] Together, these mechanisms form the basis of our modeling framework.

Connexin-based gap junctions, which permit intercellular diffusion of second messengers (notably IP_3) mediate intercellular coupling in the human lens—predominantly Cx43 in LECs and Cx50 in both epithelium and fiber cells.[16,18–20] In human LECs, purinergic pathways govern ATP/UTP-evoked Ca^{2+} responses via $P2Y_2$ receptors (particularly in the equatorial region) coupling extracellular nucleotides to IP_3-dependent ER release,[9,17,21] with similar regional enrichment reported in rat lens.[22] By contrast, P2X receptors are ionotropic and mediate rapid cation influx. Their prominence is species- and context-dependent and increases under stress and in culture.[22,23] Given that $P2Y_2$ dominates ATP/UTP-evoked responses in human LECs, we focus our paracrine analysis on P2Y-driven IP_3 production. Together with evidence that LEC-to-LEC communication supports lens homeostasis[24] and that epithelial Ca^{2+} waves can be conveyed by gap junctions and/or ATP release,[25] this design provides the lens-specific basis for the analyses that follow.

Building on our previous work demonstrating differences in intercellular Ca^{2+} wave propagation between mild and advanced stages of cataracts in human LECs,[26,27] the present study moves from phenomenological observation toward a mechanistic, model-based analysis of the underlying coupling pathways. We combine multicellular Ca^{2+} imaging of postoperative anterior LCs from patients with primary clinically mild cataracts with targeted perturbations (carbenoxolone [CBX] to reduce gap-junctional coupling and apyrase to hydrolyze extracellular ATP) and a multicellular computational model to elucidate the relative roles of gap-junctional diffusion and ATP-mediated paracrine signaling. This extends prior observations by providing a quantitative framework for how these routes jointly shape Ca^{2+} wave propagation. In the computational part of our study, we relied on the theoretical framework of Vainio et al.,[28] who developed a detailed model of Ca^{2+} signaling in the retinal pigment epithelium. We adapted the parameter set, used a tessellation-based epithelial geometry that captures realistic cytoarchitecture, and further extended the model to incorporate detailed and distinct modes of intercellular communication.

Both communication routes, gap-junctional diffusion of IP_3 and paracrine signaling via extracellular ATP, are well established in other non-excitable epithelia, including retinal pigment epithelium, airway epithelium, and the developing cochlea, and are supported by experiments[25] and mathematical models.[28–30] Their relative contributions are tissue- and context-dependent: regenerative ATP release has been reported to sustain long-range wave propagation, whereas gap-junctional diffusion often dominates over shorter ranges.[29,30] Ca^{2+} thus acts as a network-level integrator that encodes signals across space and time.[31] What remains unresolved is how these two routes combine to govern mechanically induced Ca^{2+} waves in human LECs—a question we address with our LC experiments and multicellular model.

Materials and Methods

Experimental Methods

Ethics Statement. The research followed the tenets of the Declaration of Helsinki. The study was approved by the National Medical Ethics Committee of the Republic of Slovenia, n: 0120-45/2025-2711-3, and all patients signed informed consent before the operation.

Lens Capsules Preparation. Experiments were performed on the anterior LC preparations consisting of the monolayer of LECs attached to the basal lamina (capsule matrix). The LCs were obtained routinely during cataract surgery performed at the Eye Hospital, University Medical Centre, Ljubljana, Slovenia. The central LECs were studied from the approximately 5 to 5.5 mm circles of the central anterior LCs, carefully removed by continuous curvilinear capsulorhexis. The lens capsule/epithelium originated from 20 patients aged 45 to 89 years (mean = 72 years) undergoing cataract surgery. This surgical material represents the most practical and ethically acceptable source of human lens epithelium for experimental research. Due to ethical and logistical constraints, systematic studies on non-cataractous patient tissue as well as on tissue from cadaveric donor eyes are rarely feasible. We included one rare instance, a healthy lens epithelium sample from a patient with primary posterior-segment pathology, where a combined phacoemulsification and vitrectomy was performed (with patient consent) to avoid two separate surgeries and facilitate early visual recovery. However, such cases are exceptional and unpredictable in timing, making them unsuitable for systematic investigation.

To minimize pathological confounders, only regions of the human anterior lens epithelium showing no visible damage were used in this study. Most samples originated from lenses with clinically mild cataracts; specifically, 27 of 32 experiments were performed on mild cataract lens capsule/epithelium preparations, whereas the remaining 5 (3 in control, 1 in apyrase, and 1 in CBX protocol) were obtained from lenses with advanced cataracts. After the surgery, each LC was stored in the physiological solution with (in mM): NaCl 131.8, KCl 5, MgCl2 2, NaH2PO4 0.5, NaHCO3 2, CaCl2 1.8, HEPES 10, and glucose 10, at pH 7.24, and transported at room temperature to the research

Investigative Ophthalmology & Visual Science

laboratory in the same building in approximately half an hour. Until utilization, the LCs were kept in a CO2 incubator (Innova CO-48; New Brunswick Scientific, Enfield, CT, USA) at 37°C and 5% CO2. The LCs were loaded with the AM ester of Fura-2 (Fura-2 AM; Invitrogen–Molecular Probes, Waltham, MA, USA). For loading Fura-2 AM in DMSO was suspended in 3 mL of physiological solution to a final concentration of 2 µM. The loading was done in the incubator at 37°C and 5% CO2 for 30 minutes. After loading, the LCs were washed twice for 10 minutes with fresh physiological solution. LCs were then transferred to the plastic glass bottom Petri dishes (Mattek Corp., Ashland, MA, USA; 3.5 cm in diameter) filled with 2.5 mL of the physiological solution. LCs were gently stretched by using microdissecting tweezers (WPI by Dumont, Med. Biologie, Friedberg, Germany), and then they were immobilized by a harp-like grid, a parallel array of fine nylon monofilament threads glued at approximately 500 µm intervals to a U-shaped platinum wire frame, similar to the one used for experiments with small vertebrate brain slices,[32] so that the mechanical stimulation would not displace them. The grid also flattened the LC, which was necessary for the optical recording. The orientation of the LC was with the basal lamina to the bottom, so the mechanical stimulus was applied to the LECs and not to the basal lamina. In this orientation, the applied agonist/antagonist could easily diffuse to the cells without having to cross the barrier of the basal lamina. The Petri dish with the immobilized LC was then mounted on the inverted microscope Zeiss Axiovert S 100 (Carl Zeiss, Jena, Germany). The appropriate anterior LC region was then selected based on the structural preservation of the lens epithelial layer, with preference given to areas exhibiting minimal or no signs of epithelial disruption.[33] The experiments were done at room temperature.

To test responses to mechanical stimuli, the mechanical stimulation with a tip of a glass micropipette mounted on a MP-285 micromanipulator (Sutter, Novato, CA, USA) was used. A glass micropipette was made by pulling a glass capillary (no. TW150F-3, World Precision Instruments, Sarasota, FL, USA) with a puller (P-97 Sutter Instrument, Novato, CA, USA). Prior to use, the tip of the pipette was heat-polished until it rounded up (Micro-Forge, MF-200; World Precision Instruments, USA). Using a micromanipulator and real-time visualization on a monitor connected to a video camera (12-bit cooled CCD camera SensiCam: PCO Imaging, Kelheim, Germany), the microelectrode was carefully advanced toward a single LEC until stimulation was indicated by a detectable fluorescent change, at which point the microelectrode was retracted. Mechanical stimulation was consistently performed by the same trained individual for all experimental conditions.

To study the paracrine effect of ATP on signal spreading, 8 LCs (6 of the original 20 LCs and 2 additional LCs), after the control mechanical stimulation experiment recording, were incubated for 30 minutes with apyrase (A7646; Sigma, St. Louis, MO, USA), 3 µM, at 3 µL in 2.5 mL of physiological solution, where the supplemented solution was prepared in advance and entirely replaced the old one, and then again stimulated mechanically with a micropipette, so that the effect of apyrase was compared on the same LC in the majority of LCs. Apyrase is an enzyme which hydrolyzes ATP and effectively removes ATP from the extracellular milieu. The LC epithelium originated from 8 different patients whose age was between 45 and 89 years with the average being 70 years.

To study the effect of the gap-junction blocker CBX on signal spreading, 4 of the 20 LCs were, after the control mechanical stimulation experiment recording, incubated for 15 minutes with CBX (A7646; Sigma, St. Louis, MO, USA), 2 µM, at 2 µL in 2.5 mL of physiological solution, where the supplemented solution was prepared in advance and entirely replaced the old one, and then again stimulated mechanically with a micropipette, so that the effect of CBX was compared on the same LC. The LC epithelium originated from 4 different patients whose age was between 64 and 86 years with the average being 76 years.

Calcium Imaging. Image acquisition was done with the 12-bit cooled CCD camera SensiCam (PCO Imaging, Kelheim, Germany). The software used for the acquisition was WinFluor (written by J. Dempster, University of Strathclyde, Glasgow, UK). Objectives used were: 40X/0.75 Plan-NeoFluar and 63X/1.25 oil Plan-NeoFluar (Zeiss, Jena, Germany). The light source used was XBO 75 W (Zeiss, Germany) Xe arc lamp. The light intensity was attenuated when needed with grey filters with optical densities of 0.5, 1, and 2 (Chroma, Foothill Ranch, CA, USA). The excitation filters used, mounted on a Lambda LS-10 filterwheel (Sutter Instruments Co., Novato, CA, USA), were 340 and 387 nm (Chroma, Foothill Ranch, CA, USA). The 340/387 nm ratio allowed for the visualization of the Ca^{2+} concentration changes in the cytoplasm. Image acquisition, timing, and filter wheel operation were all controlled by WinFluor software via a PCI6229 interface card (National Instruments, Austin, TX, USA). The criteria for selecting the regions for imaging were the presence of adherent cells and good cell morphology. Image frames were acquired every 500 ms, resulting in frame cycles being 1 second long (alternating 340 nm and 387 nm recording). The manual selection of individual cells (regions of interest [ROI]) and the subsequent exportation of Ca^{2+} traces were performed with ImageJ software (National Institutes of Health, Bethesda, MD, USA).

Characterization of Calcium Dynamics. Time traces from individual ROIs were analyzed offline with custom-made scripts in Python. The 340/387 nm fluorescence ratio was used to assess the Ca^{2+} concentration changes in the cytoplasm. First, all extracted Ca^{2+} traces were smoothed by applying an adjacency averaging procedure, in order to reduce the noise. Then, we defined three characteristic times for the characterization of the $[Ca^{2+}]_i$ signaling in individual LECs, as indicated in References 26 and 27. The response time of the i-th cell, $t_{res,i}$, symbolizes the time at which the cells started to respond to the mechanical stimulation. The time at which the maximal amplitude of $[Ca^{2+}]_i$ was reached is labeled with $t_{max,i}$. Last, the time $t_{half,i}$ symbolizes the half decay time, that is, the time necessary for the 340/387 ratio to decay by 50% from the maximum toward its pre-stimulation value. Based on the response time and half-decay time, we computed the signal duration of the signal in the i-th cell as follows: $\Delta t_{dur,i} = t_{half,i} - t_{res,i}$, that is, the time necessary for the signal to increase from the basal value to its maximal value, and then decrease it by 50% from the maximum toward its pre-stimulation value. Moreover, we used the absolute difference in fluorescence ratio between the basal value and maximal value as the estimation for the amplitude of the Ca^{2+} signal. In our analyses, we predominantly investigated the characteristics of Ca^{2+} signaling with regard to the distance from the point of mechanical stimulation. More specifically, we calculated the average response times, average activation times, the average signal durations, and the average relative amplitude for all cells located in a

Investigative Ophthalmology & Visual Science

ring (annulus) with a given radius. The difference between the larger and the smaller circle defining the annulus was always 25 µm. In this manner, we calculated the signal characteristics for all cells that were present with respect to stimulation point: (1) closer than 25 µm, (2) between 25 µm and 50 µm and 75 µm away, etc., as illustrated in Reference 27.

Computational Methods

The computational model developed in this study incorporates the principal molecular mechanisms involved in intracellular Ca^{2+} signaling and intercellular communication in LECs. These include both $[Ca^{2+}]_i$-on and $[Ca^{2+}]_i$-off processes as well as pathways for intercellular signal propagation. Among $[Ca^{2+}]_i$-on mechanisms, stretch-sensitive Ca^{2+} channels (SSCCs), activated by mechanical stress, mediate Ca^{2+} influx across the plasma membrane. In parallel, $P2Y_2$ purinergic receptors, triggered by extracellular ATP, initiate intracellular signaling cascades that lead to Ca^{2+} release from the ER via IP_3 receptors type 3 (IP_3R3) and ryanodine receptors (RyRs). The $[Ca^{2+}]_i$-off mechanisms involve PMCA and SERCA pumps, which actively remove free cytosolic Ca^{2+} to restore basal levels. This architecture follows established conceptual framework for epithelial Ca^{2+} signaling[28–30] but is here adapted to the specific context of human LECs and further extended to provide a more realistic representation of intercellular interactions. The key extensions concern intercellular coupling and tissue geometry: (i) LECs are connected to Voronoi-defined neighbors with area-weighted gap-junctional conductances that permit IP_3 diffusion and short-range Ca^{2+} co-diffusion; (ii) extracellular ATP is modeled as a reaction–diffusion field with first-order hydrolysis and configurable release modes (nonregenerative, partially regenerative, and fully regenerative); and (iii) wave initiation mimics localized mechanical stimulation by transiently increasing SSCC-mediated Ca^{2+} entry and triggering ATP release. Pharmacological perturbations mirror the experiments: apyrase is represented by an added exponential ATP decay term, and in CBX conditions the gap-junctional coupling was diminished. Intercellular signaling thus proceeds via two routes: gap-junctional diffusion of IP_3 (with short-range Ca^{2+} co-diffusion) between neighbors and ATP-based paracrine activation of $P2Y_2$ receptors on adjacent cells. The tissue is implemented as a spatial network of N LECs arranged by a Voronoi tessellation, which captures realistic cell-to-cell neighborhoods. Adjacent cells are connected by area-weighted gap-junctional conductances permitting IP_3 diffusion with short-range Ca^{2+} co-diffusion, whereas extracellular ATP reaction-diffusion field with first-order hydrolysis. Full equations and parameters are provided below.

Mathematical Model of Lens Epithelium Cells. Single-cell dynamics follow Vainio et al.[28] with LEC-specific parametrization. The time-dependent intracellular Ca^{2+} dynamics in individual LECs evolves according to the combined effects of several Ca^{2+} fluxes, described by the following differential Equation 1:

$$\frac{d\left[Ca^{2+}\right]}{dt} = J_{sscc} + J_{RyR} - J_{PUMP} + J_{LEAK} + J_{IP_3R_3} + J_{GJ,Ca^{2+}}, \quad (1)$$

here, J_x denotes individual Ca^{2+} fluxes, where the subscript x refers to: influx through SSCCs, release via RyR, removal by the combined Ca^{2+} pumping activity of SERCA and PMCA (PUMP), passive leakage from both the extracellular space and the ER to the cytoplasm (LEAK, treated as a constant), Ca^{2+} release through IP_3 type 3 receptors (IP_3R_3), and intercellular diffusion of Ca^{2+} through gap junctions (GJ and Ca^{2+}).

The flux through SSCCs is modelled as $J_{sscc} = k_{sscc}O_{sscc}$, where O_{sscc} denotes the proportion of channels in the open state, defined as in Equation 2[28]:

$$\frac{dO_{\text{sscc}}}{dt} = \theta k_f - \left(\theta k_f + k_b\right) O_{sscc}. \quad (2)$$

The parameter θ is dimensionless and represents the amount of stretch induced during mechanical stimulation. After stimulation, the stretch signal decays over time according to Equation 3:

$$\frac{d\theta}{dt} = -k_\theta \theta. \quad (3)$$

Stimulation started at time t_{stim} and lasted for Δt_{stim}. During this interval, cell i experienced mechanical stretch given by $\theta_i = A_\theta e^{-\alpha_\theta r_{i,\text{stim}}}$, where A_θ is the stretch amplitude, α_θ is the stretch-distance decay coefficient and $r_{i,\text{stim}}$ is the distance of cell i from the point of stimulation. Additionally, during stimulation, the cell at the point of stimulation and its immediate neighbors experienced a constant influx of IP_3 given by $k_{IP_3,\text{in}} = [IP_3]_{\text{in}}\Delta t_{\text{stim}}{}^{-1}$. After stimulation, the IP_3 influx returned to zero, and the mechanical stretch of cells relaxed according to Equation 3.

The RyR-mediated Ca^{2+} release is modeled according to Reference 34 as $J_{ryr} = k_{ryr}P_{ryr}$, where the open probability (P_{ryr}) is given by Equation 4:

$$P_{ryr} = \frac{w^\infty\left(1 + \left(\frac{[Ca^{2+}]}{K_b}\right)^3\right)}{1 + \left(\frac{K_a}{[Ca^{2+}]}\right)^4 + \left(\frac{[Ca^{2+}]}{K_a}\right)^3} \quad (4)$$

and the sensitivity function w^∞ is calculated as in Equation 5[28]:

$$w^\infty = \left(\frac{1 + \left(\frac{K_a}{[Ca^{2+}]}\right)^4 + \left(\frac{[Ca^{2+}]}{K_b}\right)^3}{1 + \frac{1}{K_c} + \left(\frac{K_a}{[Ca^{2+}]}\right)^4 + \left(\frac{[Ca^{2+}]}{K_b}\right)^3}\right) \quad (5)$$

All parameters are listed in the Table.

The combined Ca^{2+} pumping activity of SERCA and PMCA is modeled using Hill kinetics with a Hill coefficient of 2, as in Equation 6[28]:

$$J_{pump} = V_{pump}\frac{\left[Ca^{2+}\right]^2}{K_{pump}{}^2 + \left[Ca^{2+}\right]^2}. \quad (6)$$

The IP_3-induced release of Ca^{2+} from the ER via IP_3R_3 is modeled as $J_{IP_3R_3} = k_{IP_3R_3}O^4+$, where O represents the steady-state proportion of open IP_3R_3 channels (composed of 4 subunits), defined as in Equation 7:

$$O = \frac{\phi\,[IP_3]}{\frac{k_{-1}+k_2}{k_1}\phi + [IP_3]}. \quad (7)$$

Table. Model Parameters With Corresponding Descriptions and Values

Parameter	Description	Value
k_{SSCC}	Maximum flux through SSCC*	0.40 μM s^{-1}
k_f	Forward rate constant of SSCC activation*	0.20 s^{-1}
k_b	Backward rate constant of SSCC inactivation*	0.035 s^{-1}
k_θ	Relaxation parameter of induced stretch*	0.02 s^{-1}
$[IP_3]_{in}$	Total concentration if IP_3 increase of stimulated cell and its neighbors	0.5771 μM
Δt_{stim}	Duration of stimulation	2 s
A_θ	Stretch amplitude	0.4
α_θ	Stretch-distance decay coefficient	0.2 μm^{-1}
α_1	Maximal rate of k_1 for IP_3R_3 receptors	40 μM s^{-1}
β_1	$[Ca^{2+}]$ for half-maximal activation of k_1	0.8 μM
k_{deg}	IP_3 degradation rate	1.25 s^{-1}
k_{-1}	Rate for IP_3R_3 transition from open to closed state	0.88 s^{-1}
k_2	Transition rate from open to first inactivated state of IP_3R_3	0.5 s^{-1}
k_3	Transition rate from first inactivated to closed state of IP_3R_3	0.5 s^{-1}
β_4	$[IP_3]$ for half-maximal k_4	0.01 μM
k_5	Transition rate from second inactivated to closed state of IP_3R_3	0.02 s^{-1}
$k_{IP_3R_3}$	Maximum IP_3-induced Ca^{2+} flux through IP_3R_3	155.8 $\mu M s^{-1}$
K_a	Dissociation constant for RyR channel state[34]	0.37224 μM
K_b	Dissociation constant for RyR channel state[34]	0.63601 μM
K_c	Dissociation constant for RyR channel state[34]	0.05714 μM
k_{RyR}	Maximum Ca^{2+} flux through RyR	16.04 μM s^{-1}
J_{leak}	Passive Ca^{2+} leak from extracellular space and ER to cytosol	0.145 μM s^{-1}
V_{pump}	Maximum Ca^{2+} removal rate via SERCA and PMCA	5.341 μM s^{-1}
K_{pump}	$[Ca^{2+}]$ for half-maximal pump activity	0.5030 μM
ATP_0	ATP concentration released by stimulated cell*	0.061 μM
D_{ATP}	Diffusion coefficient of ATP in extracellular space	236 $\mu m^2 s^{-1}$
$[R_T]$	Total number of membrane-bound P2Y2 receptors	20,000
K_1	Unphosphorylated receptor dissociation constant*	4 μM
K_2	Phosphorylated receptor dissociation constant	100 μM
k_r	Receptor recycling rate	$1.75 \cdot 10^{-4}$ s^{-1}
k_p	Receptor phosphorylation rate	0.03 s^{-1}
k_e	Internalization rate of phosphorylated receptors	$6 \cdot 10^{-3}$ s^{-1}
ξ	Fraction of mobile receptors available for activation	0.85
$[G_T]$	Total amount of G-protein molecules	$1 \cdot 10^5$
k_a	G-protein activation rate	0.017 s^{-1}
k_d	G-protein deactivation rate	0.15 s^{-1}
$[PIP_{2,TOT}]$	Total amount of PIP_2 molecules available for hydrolysis	$5.0 \cdot 10^4$
r_r	PIP_2 replenishment rate	0.015 s^{-1}
δ	G-protein intrinsic activity parameter	$1.238 \cdot 10^{-3}$
K_3	Dissociation constant for Ca^{2+} binding to PLC	0.4 μM
α	Effective gain rate for PLC activation	$2.781 \cdot 10^{-5}$ s^{-1}
N_a	Avogadro's number	$6.02 \cdot 10^{23}$
$D_{Ca^{2+}}$	Gap junction diffusion coefficient for Ca^{2+}	512.7 $\mu m^2 s^{-1}$
D_{IP_3}	Gap junction diffusion coefficient for IP_3	913.9 $\mu m^2 s^{-1}$
$t_{apyrase}$	Time constant for extracellular ATP degradation by the enzyme apyrase	9.0 s
$\varepsilon_{IP_3} A_{i,j}$	Coupling coefficient for IP_3 between cells i and j*	0.35 – 0.45 s^{-1}
$\varepsilon_{Ca^{2+}} A_{i,j}$	Coupling coefficient for Ca^{2+} between cells i and j*	0.18 – 0.26 s^{-1}

Unless otherwise indicated (*), values are taken from Reference 28.
* Parameters fitted to experimental data.

Here, the sensitivity function ϕ, describing the response IP_3R_3 to IP_3, is given by Equation 8:

$$\phi = \frac{1}{1 + \frac{k_2}{k_3 + k_4}\left(1 + \frac{k_4}{k_5}\right)}. \quad (8)$$

The rate coefficient k_1, which controls the transition from the closed to the open state, depends on cytosolic Ca^{2+} concentration and is defined as in Equation 9:

$$k_1 = \frac{\alpha_1 [Ca^{2+}]^3}{{\beta_1}^3 + [Ca^{2+}]^3}. \quad (9)$$

The coefficient k_4, representing the rate of transition from the first to the second inactivated state, is defined as in Equation 10:

$$k_4 = \frac{\alpha_4 [IP_3]}{\beta_4 + [IP_3]}. \quad (10)$$

All parameters are listed in the Table.

The agonist-induced activation of the $P2Y_2$ receptor and the resulting second messenger (IP_3) dynamics are modeled following the approach of Vainio et al.[28] In our model, ATP serves as the ligand (L) that activates the $P2Y_2$ receptor, and its extracellular concentration as sensed by the cells is

described by Equation 19. Upon ligand binding, a fraction of $P2Y_2$ receptors on the cell surface undergoes phosphorylation at a rate k_p, leading to receptor desensitization. These phosphorylated receptors are internalized at a rate k_e, after which they are dephosphorylated and recycled back to the cell surface at a rate k_r. Only unphosphorylated receptors $[R_S]$ can activate G-proteins. The total surface receptor pool is denoted by $[R_T]$, the dissociation constant for unphosphorylated receptors is K_1, and the extracellular ligand concentration by $[L]$. The dynamics of the unphosphorylated receptor population is given by Equation 11:

$$\frac{d[R_S]}{dt} = k_r [R_T] - \left(k_r + \frac{k_p [L]}{K_1 + [L]}\right)[R_S] - k_r \left[R_p^S\right]. \quad (11)$$

The concentration of phosphorylated receptors $[R_p^S]$, governed by dissociation constant K_2, evolves according to Equation 12:

$$\frac{d\left[R_p^S\right]}{dt} = [L]\left(\frac{k_p [R_S]}{K_1 + [L]} - \frac{k_e \left[R_p^S\right]}{K_2 + [L]}\right). \quad (12)$$

Ligand binding to P2Y2 triggers activation of the enzyme phospholipase C (PLC), which hydrolyzes phosphatidylinositol 4,5-bisphosphate (PIP_2) into IP_3. The G-protein activation rate k_a is assumed to be proportional to two ratios: (i) the relative activity of ligand-bound versus unbound receptor species, denoted by (δ), and (ii) the fraction p_r of ligand-bound receptors relative to the total receptor population. G-proteins deactivate at a rate k_d. Based on that, the dynamics of the active receptor species $[G]$, as well as the ratio p_r, are given by Equations 13 and 14:

$$\frac{d[G]}{dt} = k_a (\delta + p_r)([G_T] - [G]) - k_d [G], \quad (13)$$

$$p_r = \frac{[L][R_S]}{\zeta [R_T](K_1 + [L])}, \quad (14)$$

where ξ represents the fraction of receptors that remain mobile within the membrane and are available for ligand binding.

The dynamics of IP_3 concentration is governed by its production via PIP_2 hydrolysis, degradation at rate k_{deg}, and by intercellular diffusion through gap junctions J_{gj,IP_3}, as shown in Equation 15:

$$\frac{d[IP_3]}{dt} = r_b N_a^{-1} \upsilon^{-1} [PIP_2] - k_{deg} [IP_3] + J_{gj,IP_3}, \quad (15)$$

The hydrolysis rate r_b, which regulates IP_3 production, depends on the effective signal gain parameter α and the dissociation constant K_3 for Ca^{2+} binding to PLC, as shown in Equation 16:

$$r_b = \alpha \left(\frac{\left[Ca^{2+}\right]_i}{K_3 + \left[Ca^{2+}\right]_i}\right)[G] \quad (16)$$

To maintain sustained IP_3 production during prolonged receptor activation, the model includes PIP_2 replenishment dynamics. This process is driven by the replenishment rate r_r and is constrained by the total pool of available PIP_2 $[PIP_{2,TOT}]$, as shown in Equation 17:

$$\frac{d[PIP_2]}{dt} = -(r_b + r_r)[PIP_2] - r_r N_a \upsilon [IP_3] + r_r \left[PIP_{2,tot}\right]. \quad (17)$$

The total gap junction flux $J_{GJ,X,i}$ of species X, being either Ca^{2+} or IP_3, into cell i from all its neighboring cells j is given by Equation 18:

$$J_{GJ,X,i} = \sum_j \varepsilon_x A_{i,j} \left([X]_j - [X]_i\right), \quad (18)$$

where ε_x is the per-area coupling coefficient defined as shown in Equation 19:

$$\varepsilon_X = \frac{D_X a_p \rho_{gj}}{\zeta V}, \quad (19)$$

which combines the diffusivity D_X of species X (Ca^{2+} or IP_3) in the junction pore, the single-channel cross-sectional area a_p, the gap-junction channel density ρ_{gj}, the effective pore length ζ, and the receiving cell's volume V. In Equation 18, $A_{i,j}$ denotes the surface area of the shared boundary between cells i and j.

Cells also engage in paracrine interactions mediated by extracellular ATP diffusion. We consider three modes of paracrine communication: (i) non-regenerative, where only the initially stimulated cell releases ATP, (ii) partially regenerative, where each activated cell releases ATP, but the amount decreases with increasing distance from the stimulation site, and (iii) fully regenerative, where each activated cell releases the same amount of ATP regardless of location. The combined ATP concentration sensed by cell i (ATP_i) at time t, due to diffusion from all secreting cells j, and as a function of distance $r_{i,j}$ is described by Equation 20:

$$ATP_i(r,t) = \sum_j \frac{ATP_{0,j}}{\sqrt{4\pi D_{ATP}\left(t - \tau_j\right)}} e^{-\frac{r_{i,j}^2}{4D_{ATP}\left(t-\tau_j\right)}}, \quad (20)$$

where $ATP_{0,j}$ is the concentration of ATP released from the activated cell j, D_{ATP} is the diffusion coefficient of ATP in the extracellular space, and τ_j is the activation time of the secreting cell j.

Model parameter values used in our simulations, along with their descriptions, are listed in the Table. For further methodological details, we refer to the original work of Vainio et al.[28] In addition to LEC-specific modifications, some parameter values were adjusted relative to the original model to better reflect values reported for LECs in the literature and to ensure consistency with our experimental observations.

Multicellular Network of Lens Epithelium Cells. To construct a realistic model of the epithelial monolayer, we used Voronoi tessellation, a method that is commonly used to construct planar tissues,[35] including the epithelial layers.[36] First, the planar domain was populated with randomly distributed seed points with predefined minimal inter-seed distance. This constraint ensured cell surface areas consistent with typical size of human LEC (9–17 µm diameter[37]). These diameters correspond to cross-sectional cell areas ranging from approximately 45^2 to 75 μm^2. The generated seed points were taken as the cell

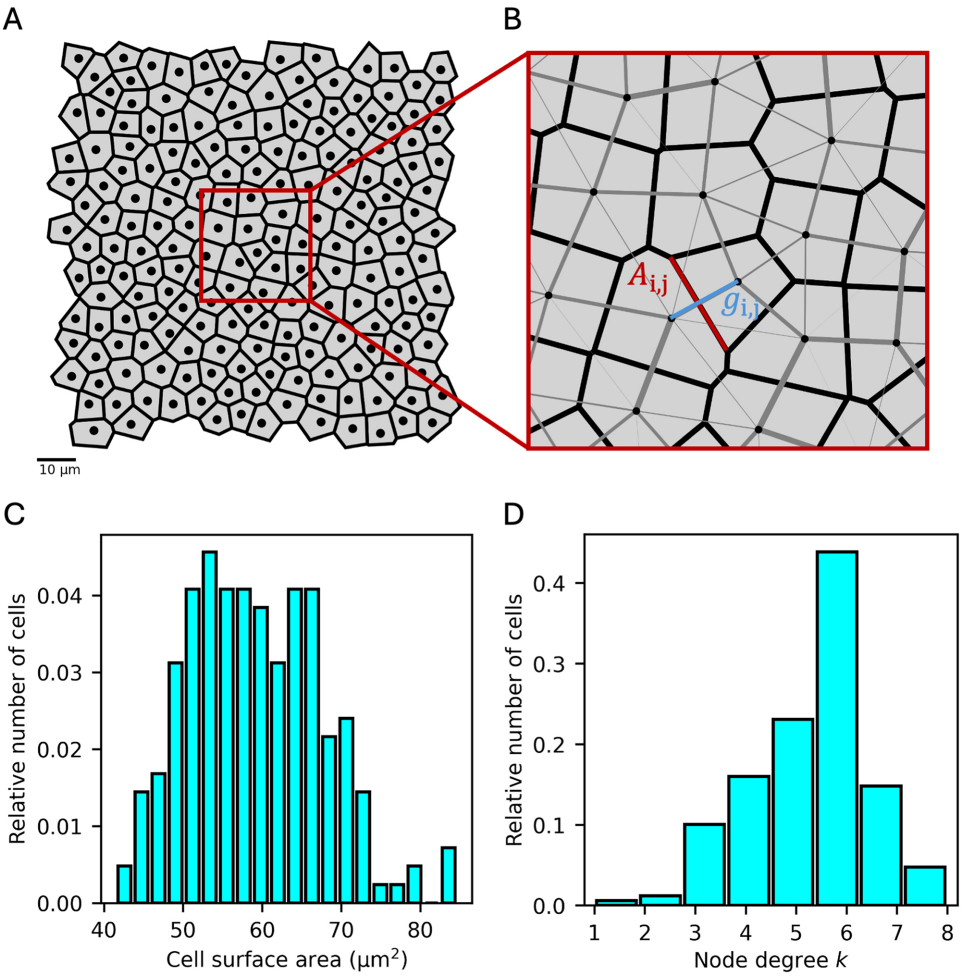

Figure 1. Model of the intercellular network of LECs. (**A**) A typical Voronoi-generated LEC network. *Black lines* indicate cell borders and *black dots* represent the center of individual cells (*left*). (**B**) The *right panel* shows the zoomed-in section of the network with superimposed intercellular connections (*gray lines*). The *thickness* of the *gray lines* reflects the relative strength of intercellular coupling. Connectivity between cells *i* and *j* is highlighted by a *light blue line* ($g_{i,j}$), whose thickness corresponds to the area of their shared cell wall $A_{i,j}$ (*red line*). (**C**) Distribution of cell surface areas in the network. (**D**) Distribution of node degrees (k), that is, the number of connections per cell. The average node degree is $\langle k \rangle = 5.5$.

centers (centers of mass) for the LECs, and the surrounding space was partitioned using Voronoi tessellation, resulting in a morphologically realistic planar epithelial network (Fig. 1A, left).

We then establish intercellular connections, that is, gap junctions, based on the shared borders between neighboring cells. If two cells, that is, cell *i* and cell *j*, share a common wall, they are considered connected, and the strength of their connection is determined by the area of the shared membrane surface, denoted by $A_{i,j}$ (Fig. 1A, right). The resulting epithelial network comprises a $N = 225$ cells (see Fig. 1) and exhibits a near-normal distribution of cell surface areas, with an average area around $\langle A \rangle = 60\,\mu m^2$, corresponding to a typical cell diameter of approximately 9 µm (see Fig. 1B). The distribution of node degrees, that is, the number of intercellular connections per cell, is somewhat heterogenous, with nearly half of the cells having six neighbors (see Fig. 1C). The volumes of the generated LECs were calculated such that the average cell volume approximates 570 μm^3, implying an effective cell height of approximately 9 µm. To further refine the model, we adjusted intercellular coupling strength by incorporating the average membrane surface area occupied by gap junctions (3.36 ± 0.38%),[38] in combination with the area of the shared cellular interfaces.

Modeling the Effects of Apyrase and Carbenoxolone. To model ATP inhibition by the enzyme apyrase, Equation 20 is modified as Equation 21:

$$ATP_i(r,t) = \sum_j \frac{ATP_{0,j}}{\sqrt{4\pi D_{ATP}(t-\tau_j)}} e^{-\frac{r_{i,j}^2}{4D_{ATP}(t-\tau_j)}} e^{-\frac{\Delta t_{act,j}}{t_{apyrase}}}, \quad (21)$$

where the additional exponential factor on the right-hand side accounts for the time-dependent degradation of ATP released by cell *j*, mediated by apyrase. Here, $t_{apyrase}$ denotes the characteristic time of extracellular ATP degradation, and $\Delta t_{act,j}$ is the time elapsed since activation of cell *j*. The enzyme is assumed to be uniformly distributed in the extracellular medium. To simulate the effect of CBX, a potent gap-junction inhibitor that blocks connexin-mediated intercellular communication, we abolished the intercellular gap junctional conductance for both Ca^{2+} and IP_3 to levels that mimic the experimentally observed effects of CBX.

Results

Experimental Results

We experimentally examined the spatial propagation of mechanically induced Ca^{2+} signals in LECs from human postoperative anterior LC preparations consisting of the epithelial monolayer of LECs attached to the basal lamina under control conditions, as well as after treatment with the ATP-hydrolyzing enzyme apyrase or the gap-junction blocker CBX, as shown in Figure 2A–C, respectively. Ca^{2+} concentrations are represented as 340 of 387 ratio images, superimposed on images recorded at 340 nm to allow visualization of individual LEC positions. Under control conditions (see Fig. 2A), LECs exhibited a transient increase in intracellular Ca^{2+} that propagated radially from the stimulation site as a wave, encompassing nearly all cells in the field of view. In most cases, the centrally stimulated cell was visibly damaged or non-viable due to the applied mechanical force, whereas surrounding LECs in the immediate annulus were likely still directly affected by the stimulus. In contrast, more distant cells—beyond the range of direct mechanical influence—could only respond via intercellular signaling mechanisms. In apyrase-treated LC (see Fig. 2B), a propagating Ca^{2+} wave was still observed, although its propagation range was notably reduced compared to the control LC. In CBX-treated LC (Fig. 2C), Ca^{2+} increases were limited to cells adjacent to the stimulation site, and no intercellular Ca^{2+} wave was observed. In the latter case, notably, even neighboring LECs that are normally functionally coupled to the stimulated cell via gap junctions failed to respond. The corresponding experiments are shown in Supplementary Videos S1 (control), S2 (apyrase), and S3 (CBX), which provide dynamic visualizations of the Ca^{2+} activity described in Figure 2.

To visualize the spatiotemporal profiles of Ca^{2+} transients after mechanical stimulation in the LC more explicitly, Figure 3 shows the corresponding normalized Ca^{2+} traces (upper panels) along with a spatial map of responsive LECs (lower panel). Ca^{2+} signals from individual LECs are presented as normalized 340 of 387 ratio time series, arranged according to the distance from the stimulation site (denoted with an X in the lower panel). In the lower panel, LECs that exhibited a detectable Ca^{2+} increase, are marked with black circles, whereas unresponsive cells are indicated by open circles. It can be observed that the propagation range of the Ca^{2+} wave was reduced in the apyrase-treated condition, and that CBX treatment abolished intercellular wave propagation across the tissue.

To gain a general insight, we quantified the spatiotemporal Ca^{2+} activity and pooled data from multiple LCs. The results in Figure 4 illustrate how the fraction of activated cells and various Ca^{2+} signaling characteristics vary with distance from the stimulation site across different experimental conditions. Specifically, the plots represent average values from multiple LCs, calculated for all cells located within a given radial distance interval (annulus; see Materials and Methods). In Figure 4A, it can be seen that the fraction of activated cells gradually decreases with increasing distance from the stimulation point in both control and apyrase-treated LCs. However, the decline is significantly more pronounced under apyrase conditions, as 96% of LECs were activated at 100 µm from the stimulation

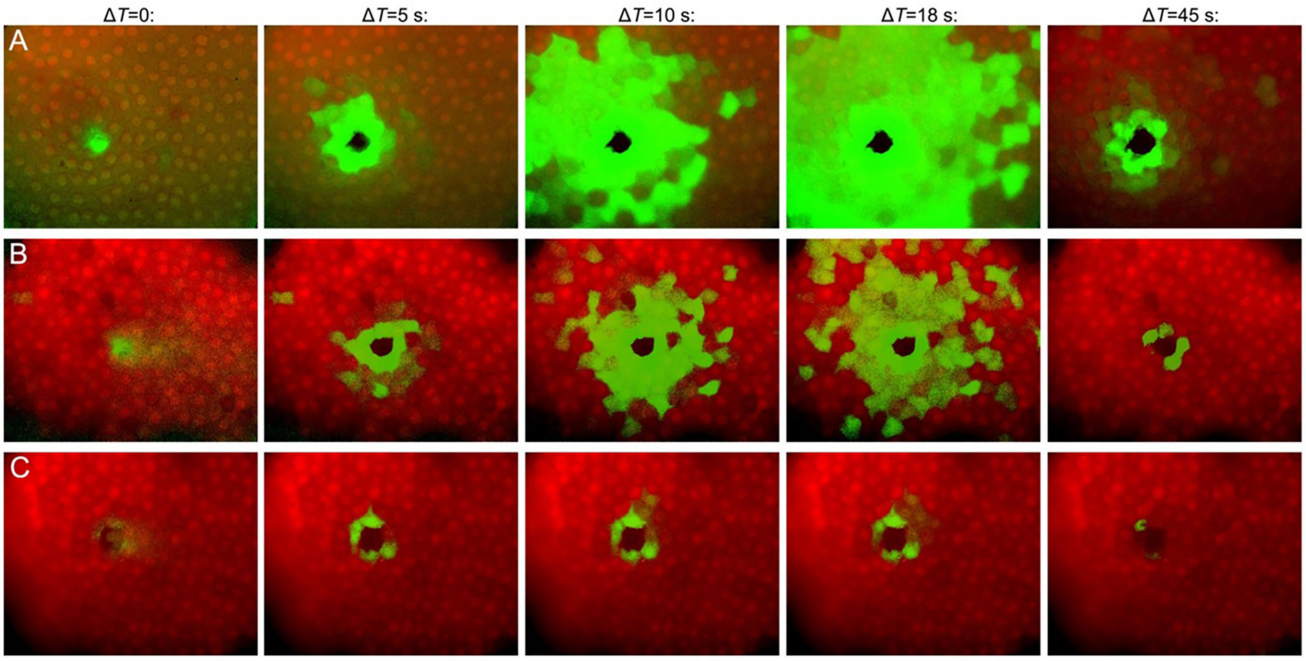

Figure 2. Spatiotemporal patterns of Ca^{2+} responses in in LECs from human postoperative anterior LC preparations consisting of the epithelial monolayer of LECs attached to the basal lamina following local mechanical stimulation for a typical control experiment (**A**), for a typical experiment in which the LCs were preincubated for 30 minutes with the ATP hydrolyzing enzyme apyrase (3 µM) (**B**), and for a typical experiment in which the LCs were pre-incubated for 15 minutes with the gap-junction blocker CBX (2 µM) (**C**). The plots show a series of 340 of 387 ratio images superimposed on anterior LC images recorded at 340 nm at the indicated time points, whereby green colors indicate elevated Ca^{2+} concentrations.

Investigative Ophthalmology & Visual Science

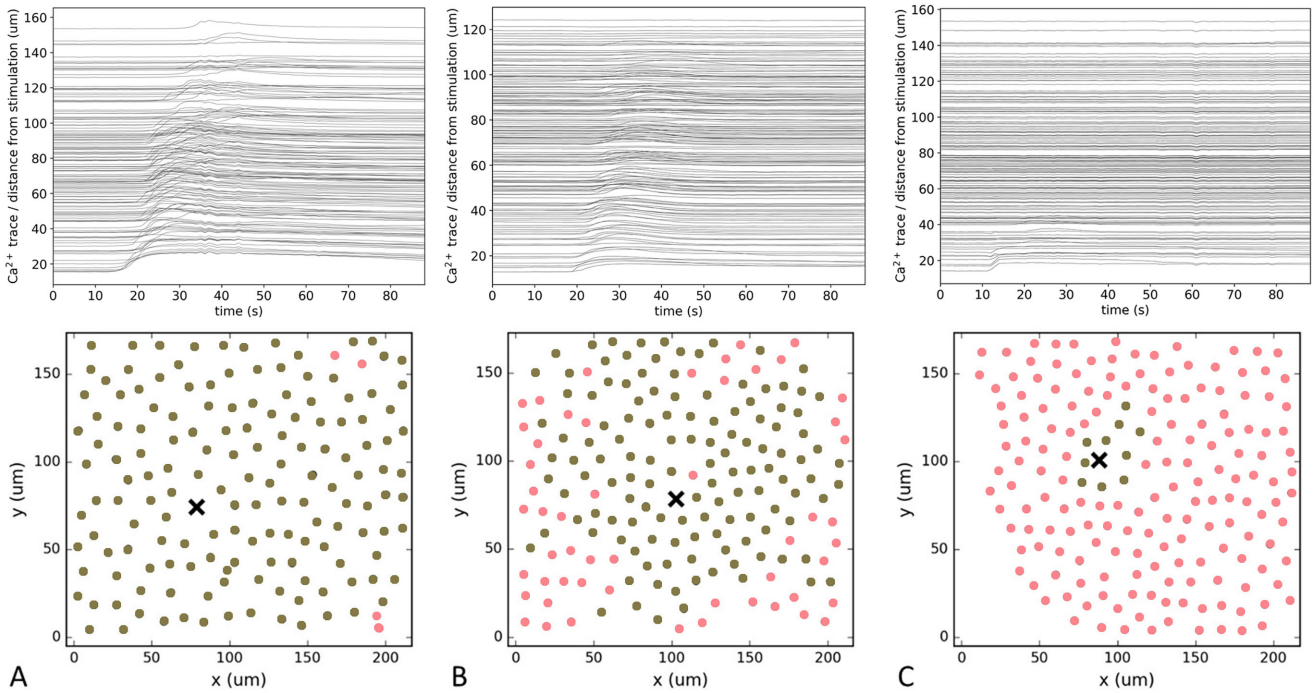

Figure 3. Visualization of the spatiotemporal Ca^{2+} activity of LECs in the same representative LC recordings shown in Figure 2: under control conditions (**A**), and in experiments where LCs were pre-incubated for 30 minutes with 3 µM apyrase (**B**) or 15 minutes with 2 µM CBX (**C**). The *upper panels* show normalized 340 of 387 ratio traces for individual LECs, arranged according to their distance from the stimulation site (marked with a *black X*). The *lower panels* display individual LECs as *black circles* if Ca^{2+} concentration increased during the experiment, and as *red circles* otherwise.

site under control conditions, compared with only 73% under apyrase conditions. In CBX-treated LC, the propagation range of the intercellular Ca^{2+} wave was substantially reduced, with fewer than 20% of LECs activated at a distance of just 50 µm. Due to the low number of responsive cells, further analysis of Ca^{2+} signal characteristics in CBX-treated LC was not performed. Overall, the properties of Ca^{2+} transients followed a similar trend in both the control and apyrase-treated groups. The time lags following mechanical stimulation, reflected by the average response times, were nearly identical in both groups. This indicates that apyrase treatment does not affect the propagation velocity of Ca^{2+} waves, supporting our previous findings based on a smaller dataset.[27] In all experiments, care was taken to stimulate a single cell; however, in practice, the mechanical perturbation may occasionally activate several neighboring cells simultaneously. To avoid overestimating the apparent propagation speed due to such co-activation, we compensated for this effect in the analysis by averaging the activation times of all cells within 25 µm of the stimulation site and setting this value to zero. Additionally, the duration of Ca^{2+} transients decreased with increasing distance from the stimulation site and was consistently longer in control LC than in apyrase-treated LC, including in the cells next to the site if under mechanical stimulation. Last, the amplitude of Ca^{2+} transients also decreased with increasing distance from the stimulation site in both experimental groups. Although amplitudes in the control group were on average 10% to 20% higher than those in the apyrase group, the difference was found to be statistically significant only in the proximity of the stimulation site.

Computational Results

We used a computational model of coupled LECs to investigate mechanically stimulated Ca^{2+} signaling and the propagation of intercellular Ca^{2+} waves. The model integrates intracellular Ca^{2+} dynamics, intercellular communication via gap junctions, and paracrine signaling through ATP diffusion. It is based on biophysically grounded mechanisms and reflects the spatial organization of LECs in a realistic epithelial network. To explore the role of extracellular ATP in signal propagation, we simulated three distinct types of paracrine signaling: (i) a point-source diffusion model, (ii) a partially regenerative diffusion model, and (iii) a fully regenerative diffusion model. Each of these models reflects a different mechanism of ATP release and diffusion, enabling us to examine how variations in ATP dynamics affect Ca^{2+} signaling in the LEC network. Simulations were conducted under control conditions and two types of perturbations: apyrase treatment, in which extracellular ATP degradation was introduced to disrupt paracrine signaling, and CBX treatment, in which gap junctional coupling was inhibited. By systematically varying these conditions, we identified the specific contributions of ATP-mediated paracrine signaling and gap junctional communication that best reproduce experimental observations. These results highlight the distinct and complementary roles of both pathways in shaping the spatial and temporal dynamics of Ca^{2+} responses in the lens epithelium.

In our simulations, we modeled the lens epithelium as a network of 225 LECs and applied mechanical stimulation to the central cell at 15 seconds. The simulation results are presented in Figure 5. Figure 5A illustrates the outcome of

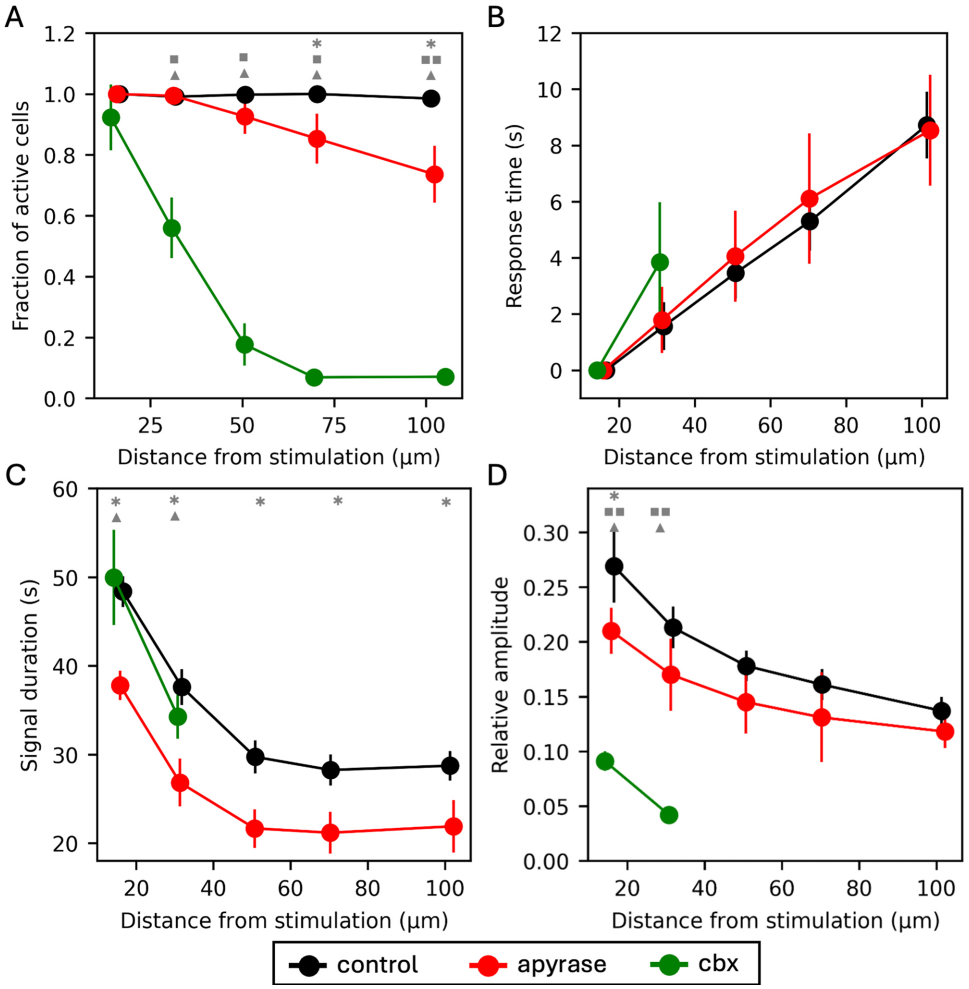

Figure 4. Quantification of Ca^{2+} signaling in LECs under different experimental conditions applied to the LC. Fraction of activated LECs (**A**); differences in response times to stimulation (**B**); signal duration times (**C**); and relative amplitudes (**D**) are shown for the control experiment (*black*), and for the experiment in which LC was preincubated with apyrase (*red*) or CBX (*green*), plotted as a function of distance from the stimulation site. Note that due to weak responses, only the fraction of activated cells was analyzed for CBX-treated LC. Data were pooled from the following number of LC: 8 (control), 7 (apyrase), and 7 (CBX). Statistical significance is indicated by symbols: * control versus apyrase; ■ control versus CBX; ▲ apyrase versus CBX (one symbol for $P < 0.05$ and two symbols for $P < 0.01$; Mann-Whitney *U* test).

the point-source diffusion model, where ATP is released exclusively from the stimulated cell and passively diffuses through the extracellular space. In this scenario, only a small proportion of cells in the immediate vicinity of the stimulated cell exhibit activation. This suggests that passive ATP diffusion, even when combined with gap-junctional coupling, is insufficient to support robust long-range propagation of Ca^{2+} waves across the epithelium. Therefore, we did not pursue further simulations with this model and instead adopted the partially regenerative diffusion model. The corresponding results are shown in the middle panel (see Fig. 5B). Under control conditions, the mechanically induced Ca^{2+} wave propagated gradually across the entire tissue, qualitatively resembling the experimental observations (see Figs. 2A and 3A). We then simulated two perturbed conditions. In the apyrase simulation, which mimics enzymatic degradation of extracellular ATP, we observed a gradual attenuation of the Ca^{2+} signal amplitude with increasing distance from the stimulation site and a decrease in the propagation range of the wave – consistent with experimental results (see Figs. 2B, 3B). The simulation resembling treatment with CBX, which disrupts gap-junctional communication, resulted in spreading of the initial Ca^{2+} signal only to a limited number of adjacent cells, closely resembling experimental outcome (see Figs. 2C, 3C). These results underscore the essential role of IP_3 and Ca^{2+} diffusion through gap junctions in facilitating spatial signal propagation across the epithelium. Next, we simulated the fully regenerative diffusion model. Under control conditions, this model produced a well-coordinated and relatively rapid Ca^{2+} wave propagation that encompassed nearly the entire tissue (see Fig. 5C). Notably, the same model exhibited robust wave propagation even under apyrase condition, indicating that the regenerative ATP release mechanism can overcome enzymatic degradation. However, under CBX conditions, the simulated wave slowed considerably with radial distance, and its amplitude was significantly reduced. Although these partially reproduced experimental observations, it diverged in one important aspect: the simulated Ca^{2+} signal did not diminish rapidly in the vicinity of the stimulated cell, unlike what was

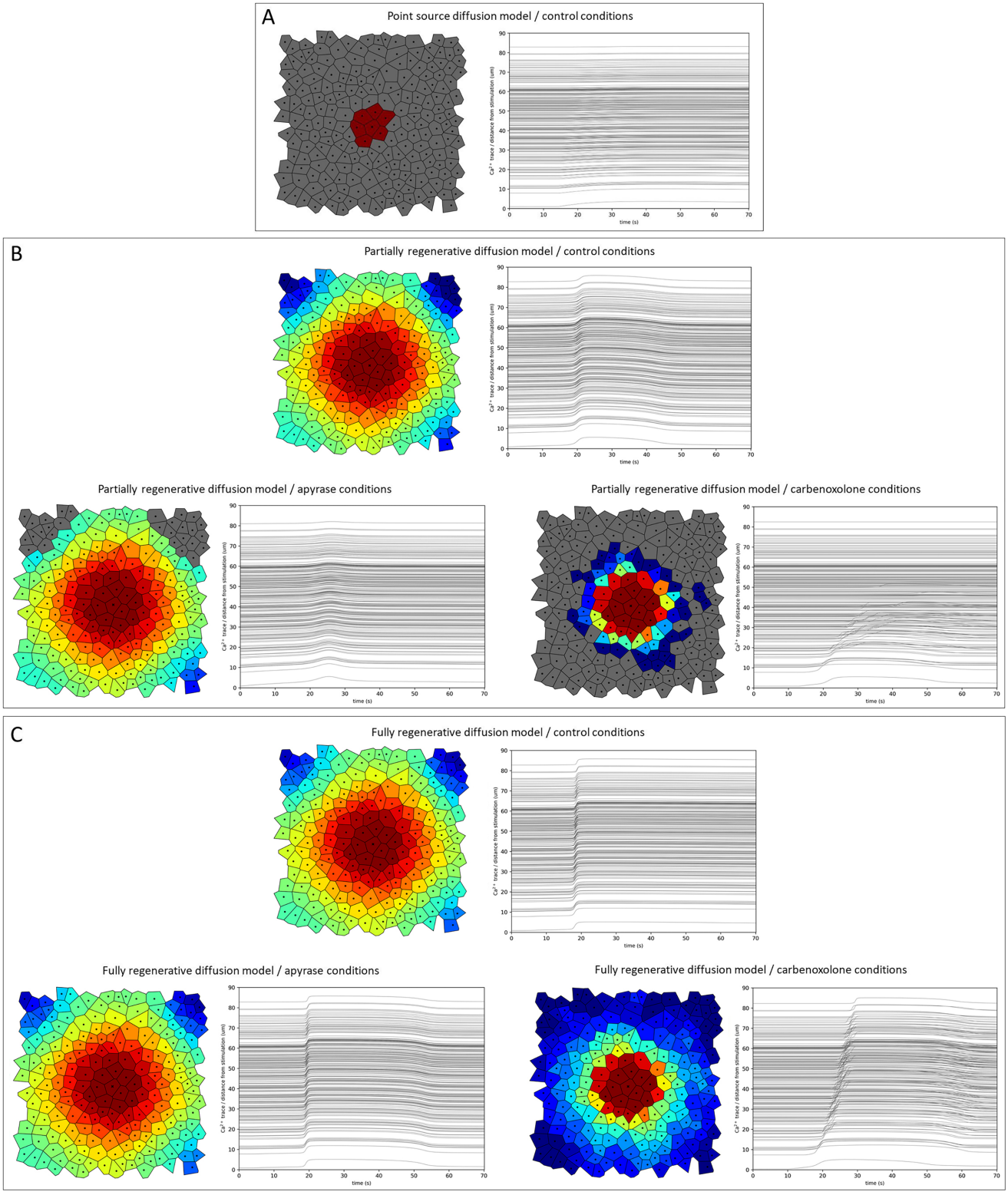

Figure 5. Numerical simulation of Ca^{2+} wave propagation for the point-source model (**A**), partially regenerative model (**B**), and fully regenerative model (**C**). For each model, simulations were performed under control conditions (*middle panels*), where both paracrine ATP signaling and gap junctional coupling were active. For the partially and fully regenerative models, additional simulations were conducted under apyrase treatment (*left panels*), which inhibits paracrine ATP signaling, and under CBX treatment (*right panels*), which blocks gap-junctional communication. In the schemes of the LEC network, cells are color-coded based on their response time: *red* indicates 0 seconds, whereas *dark blue* denotes a delay of 8 seconds or more. *Gray* marks the cells that remained inactive. The corresponding graphs on the right display Ca^{2+} traces for all individual LECs, sorted by their distance from the stimulation site.

Investigative Ophthalmology & Visual Science

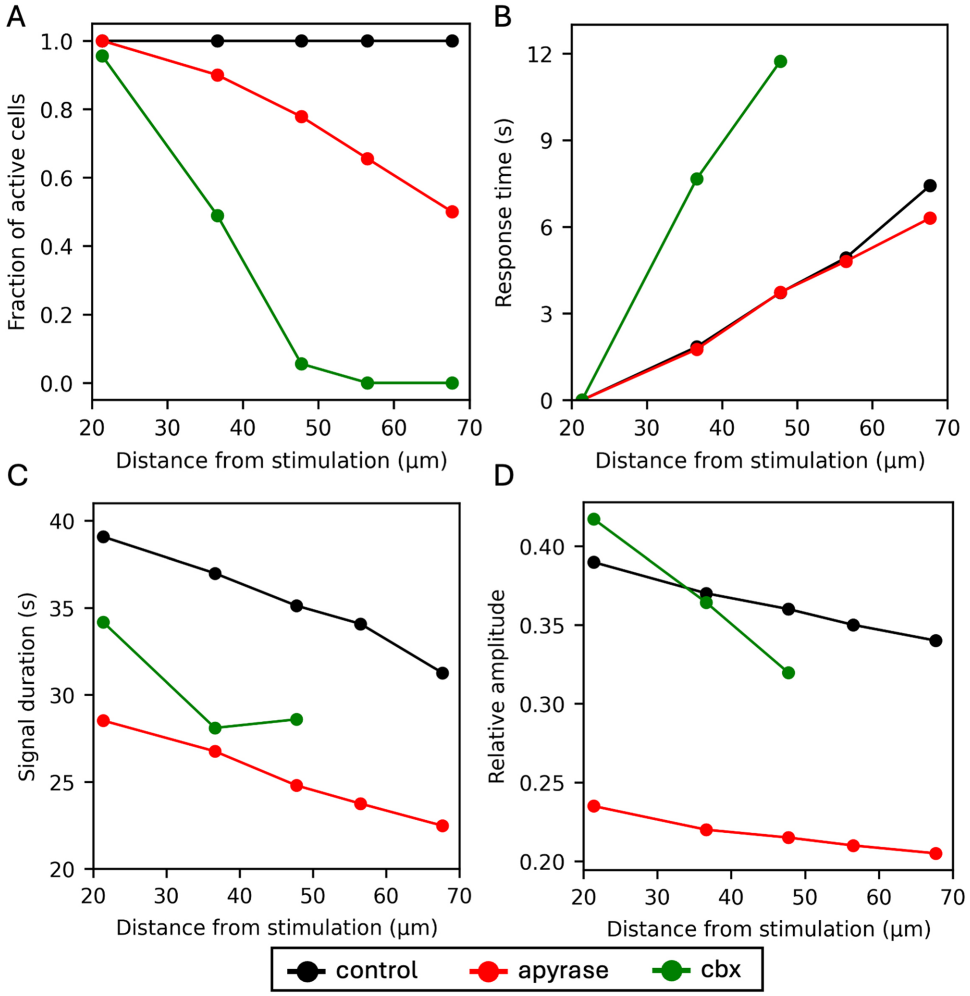

Figure 6. Quantification of Ca^{2+} signaling dynamics in LEC networks on numerical simulations. (**A**) Fraction of activated LECs; (**B**) differences in response times following mechanical stimulation; (**C**) durations of Ca^{2+} transients; and (**D**) signal amplitudes – shown as a function of distance from the stimulation site under control conditions (*black*), apyrase treatment (*red*), and CBX treatment (*green*). The data corresponds to the simulation results of the partially regenerative diffusion model presented in Figure 5B.

observed in CBX-treated experimental preparations. Based on these results, we conclude that the partially regenerative model provides the best agreement between simulations and experimental data. Supplementary videos showing simulated Ca^{2+} dynamics in the LEC network following mechanical stimulation are available for control conditions (Supplementary Video S4), apyrase treatment (Supplementary Video S5), and CBX treatment (Supplementary Video S6).

Next, we assessed the quantitative agreement between the model and experimental results, focusing on the partially regenerative diffusion model, as it showed the best qualitative consistency with experimental observations in earlier analyses. As in the quantification of experimental data, we analyzed four key parameters derived from the simulations: (i) the proportion of activated cells as a function of their distance from the stimulation site, (ii) the response times of individual LECs, which were used to estimate the propagation velocity of the Ca^{2+} wave, (iii) the duration of Ca^{2+} transients, and (iv) the amplitudes of these transients. The results, showing average values for individual LECs grouped by distance from the stimulation site, are presented in Figure 6. From Figure 6A, we observe that under apyrase conditions, the spatial range of the Ca^{2+} wave progressively decreases beyond a distance of 50 μm. In contrast, CBX treatment drastically reduces the wave's propagation range, with less than 10% activated cells beyond the 45 μm range. As shown in Figure 6B, which presents the response times as a function of distance from the stimulation site, inhibition of paracrine ATP signaling has minimal effect on the propagation velocity of the wave, which remains approximately 10 μm/s—consistent with values observed experimentally under both control and apyrase conditions. Figure 6C indicates that the addition of apyrase as well as CBX shortens the duration of Ca^{2+} transients. Finally, Figure 6D illustrates the amplitude of Ca^{2+} signals. Under apyrase treatment, amplitudes are reduced compared with control conditions. In summary, the simulation results exhibit good quantitative agreement with the experimental data across all measured parameters, supporting the conclusion that the partially regenerative diffusion model best accounts for the underlying mechanisms of intercellular signaling in the lens epithelium.

In addition to these findings, we also examined how variability in the mechanical stimulation, an inevitable feature of the experimental setup, might influence the observed responses. Although stimulation was consistently applied with the aid of a micromanipulator, some variability in the effective strength and duration of the stimulus cannot be fully excluded. To assess the potential impact of this factor, we used our computational model to simulate responses under conditions where the intensity of mechanical stimulation was either increased or decreased by 25% reflected in both strength and duration. The results, presented in Supplementary Figure S1, show that such variations have only minor effects under control and CBX conditions, whereas responses under apyrase treatment exhibit somewhat greater dispersion. Importantly, however, the principal findings remain unchanged: gap-junctional coupling continues to dominate intercellular communication, and the relative roles of paracrine ATP signaling and direct coupling are preserved irrespective of stimulation variability.

Discussion

Research into intercellular communication and the propagation of mechanically induced Ca^{2+} waves has been ongoing for over 3 decades.[39,40] This effort reflects the view that cellular responses to environmental perturbations are collective processes shaped by multicellular interactions,[41] and it remains central to understanding how cell–cell coupling governs tissue-level signaling in physiology and disease.[42–44] This is particularly relevant also for LECs, where intercellular Ca^{2+} waves could coordinate epithelial responses to external stimuli and help maintain lens integrity and function under stress; however, this remains to be established and warrants further study. Nevertheless, this protective mechanism can be disrupted: osmotic imbalance can cause cellular swelling and Ca^{2+} overload, activating pathological cascades.[45] Mechanical stress triggers analogous pathways: lens-cell sensitivity to mechanical stimulation has been demonstrated in ovine LECs,[46] and traumatic cataracts from physical injury are documented.[47] Similarly, ophthalmic surgical manipulations can impose mechanical stress on the LC and epithelium with potential downstream effects on transparency. Thus, both osmotic (metabolic) and mechanical insults converge on cellular swelling and ion dysregulation as key mechanisms in cataractogenesis.

Effective signaling between LECs facilitates the regulation of ionic balance and homeostasis within the lens, helping to preserve its transparency and reducing the risk of cataract formation.[3,12] Disruption of Ca^{2+} homeostasis has been identified as an early driver of cataractogenesis,[9,10] which motivated us to investigate intercellular signaling mechanisms in greater detail. To this end, we studied mechanically induced Ca^{2+} dynamics in human LEC monolayers obtained from postoperative anterior LC preparations from patients with primary, clinically mild cataracts. Access to non-cataractous human lens epithelium is limited for ethical and logistical reasons: anterior LC tissue is collected during cataract surgery, and non-cataractous capsules become available only rarely (e.g. during combined posterior-segment surgeries), which is insufficient for systematic study. Donor eyes constitute a potential source, but availability, postmortem delay, and tissue quality frequently preclude use at the required scale. Consequently, cataract-derived LC specimens currently provide the most feasible human tissue model. In all experiments, we restricted analyses to regions where the epithelial monolayer was morphologically intact, with no visible disruption of the epithelial layer (criteria as in Andjelić et al.[33]). These preparations provide a physiologically relevant model compared with cultured LECs, while still permitting disease-related insights. To further assess robustness, we analyzed responses in a small number of samples from advanced cataracts. As shown in the supplementary material (Supplementary Fig. S2), the qualitative behavior of Ca^{2+} signaling remained comparable, supporting the generality of our findings across cataract stages. In addition, we provide as supplementary evidence a rare control recording from a non-cataractous LC (Supplementary Fig. S3). These data are limited to a single experiment under control conditions and is included solely to illustrate that the qualitative features of the response and the key mechanisms under investigation, are not essentially different in non-cataractous tissue. Although such material is far too scarce to allow systematic quantification, this example further supports the notion that our conclusions capture general mechanisms of intercellular communication. By combining these experimental observations with multicellular computational modeling, we demonstrate that both gap-junctional coupling and a partially regenerative ATP-based paracrine diffusion mechanism contribute to Ca^{2+}-wave propagation, with gap junctions playing the dominant role under our conditions.

Across epithelia, intercellular Ca^{2+} waves use two routes whose balance is tissue-specific. Following focal injury, keratinocyte and MCF-10A models implicate point-source ATP diffusion with little gap-junctional contribution.[48,49] By contrast, retinal pigment, liver, and alveolar epithelia exhibit gap-junctional coupling acting in concert with purinergic signaling,[50–52] and in airway epithelium, local ATP release can initiate regenerative waves.[39] Consistent with this heterogeneity, our data are compatible with a lens-specific hybrid mechanism in which gap junctions dominate short-range transmission, whereas ATP-based paracrine signaling via P2Y receptors modulates spatial reach and duration: in our LC preparations, apyrase curtailed wave extent without abolishing nearest-neighbor responses, whereas CBX reduced both local transmission and longer-range recruitment — consistent with gap-junctional IP_3 diffusion as the primary conduit and ATP-based signaling as amplification. Importantly, aside from the reduced spatial reach, the qualitative nature of the signals under paracrine inhibition did not markedly change: transients were somewhat shorter in duration and exhibited lower amplitudes, in agreement with our earlier findings.[27]

These findings highlight the existence of hybrid signaling strategies across epithelial systems and suggest that tissue-specific combinations of junctional and paracrine mechanisms are functionally used. This provides a natural foundation for integrating experimental data with theoretical modeling. Theoretical modeling has long played a central role in deciphering intercellular Ca^{2+} signaling and Ca^{2+} wave propagation, with numerous studies examining how different pathways interact in multicellular systems.[53–56] Intercellular Ca^{2+} signaling in the lens epithelium fits within a broader framework of non-excitable tissue physiology, where similar mechanisms govern coordinated cellular responses. In different epithelial systems Ca^{2+} waves are mediated by gap-junctional IP_3 diffusion or by ATP-triggered paracrine signaling via purinergic receptors, and computational studies consistently find that dual-pathway architectures better reproduce experimental observations than single-mechanism models. In airway epithe-

Investigative Ophthalmology & Visual Science

lium, long-range spread requires a regenerative extracellular ATP source,[30] whereas in keratinocytes a partially regenerative ATP release suffices.[57] In ARPE-19 cells, reproducing the measured wave dynamics requires junctional diffusion of IP_3 (with short-range Ca^{2+} co-diffusion) together with extracellular ATP signaling via purinergic receptors.[28] In the developing cochlea, self-regenerative ATP release maintains propagation over extended spatial domains.[29] Collectively, these studies point to a conserved yet tissue-specific signaling logic in non-excitable epithelia: gap junctions support fast, local transmission, whereas ATP release recruits more distant neighbors. Parallel insights from astrocyte networks show that paracrine ATP alone can sustain long-range Ca^{2+} waves,[58] whereas gap-junctional IP_3 diffusion can suffice when nonlinear amplification is included.[54,59,60] More integrative models argue for complementary, context-dependent roles—gap junctions enabling rapid short-range spread and extracellular ATP supporting regenerative long-range recruitment[61,62]; adding extracellular ATP to junctional models extends range and duration without increasing speed.[63]

Our findings also align with the early experimental observations of Churchill et al.,[46] who described two scenarios for mechanically induced Ca^{2+} signaling in cultured ovine LECs depending on whether membrane integrity was preserved. First, when the plasma membrane remained intact, an intracellular second messenger was generated and propagated via gap-junctional diffusion, eliciting Ca^{2+} release from internal stores in adjacent cells – consistent with the observed exponential decay of Ca^{2+} transient amplitudes with distance from the stimulus site. Churchill et al.[46] did not identify the second messenger directly; the pattern is consistent with IP_3 diffusion but does not prove it. In our model, the junctional messenger is represented as IP_3, with co-diffusion of Ca^{2+} contributing at short range. Importantly, this scenario does not exclude regenerative amplification along the junctional pathway. Second, when the membrane was compromised, mechanical stimulation caused nonspecific plasma-membrane permeability, Ca^{2+} influx, and release of cytosolic components into the extracellular space, which were proposed to act as diffusible extracellular signaling mediators that stimulated surrounding intact cells and induced Ca^{2+} release from their stores. In that case, the extracellular mediators would presumably activate purinergic receptors on neighboring cells, leading to subsequent IP_3 production. In most of our experiments, the centrally stimulated LEC was often visibly damaged, whereas LECs in the immediate annulus remained morphologically intact yet showed clear Ca^{2+} transients. Apyrase curtailed wave extent without abolishing nearest-neighbor responses, whereas CBX reduced both local transmission and longer-range recruitment, a pattern consistent with a hybrid mechanism in which gap-junctional IP_3 diffusion provides the primary conduit for short-range transmission and ATP-based paracrine signaling via P2Y receptors supplies spatial amplification. We recognize that our experiments were performed under conditions that could be described as an "injury-on-injury" model (surgically excised LC combined with local mechanical stimulation). Such circumstances are difficult to avoid, as anterior capsule tissue can only be obtained surgically, whether from patients, donor eyes, or animal models, whereas cultured LECs lack native intercellular junctions. To minimize this limitation, we selected regions of the capsule where the epithelial layer was structurally maintained and with no visible damage (see Ref. 33). Importantly, CBX is not perfectly specific and may influence channels beyond connexins, potentially underestimating the paracrine contribution. CBX is known to interact with pannexins,[64] reducing Pannexin 1-mediated ATP release. Finally, whereas Churchill et al.[46] studied cultured ovine cells without intact architecture, our human LC preparations maintain epithelial organization, which may explain differences in pathway contributions. Taken together, we interpret the observed dominance of gap-junctional coupling as representative under our conditions, while acknowledging that the balance between junctional and paracrine mechanisms may shift with injury severity and context.

At the lens scale, a conceptual clearance scheme proposes that Ca^{2+} enters through extracellular spaces, diffuses into fiber cells along its electrochemical gradient, and returns to the surface via intercellular gap junction coupling, with active extrusion concentrated in the epithelium (PMCA and NCX) and largely absent in deeper fibers.[10,65] Within this framework, compromised efflux would be expected to promote Ca^{2+} accumulation in the lens core;[10,65] in turn, calpain (Lp82)–mediated proteolysis of crystallins has been implicated in cataract initiation.[45] This lens-scale perspective provides context for considering epithelial intercellular coupling as a relevant factor. However, there is the regional heterogeneity within the lens epithelium with the functionally and structurally distinct LECs at the periphery compared to anterior lens epithelium. Peripheral LECs, characterized by greater proliferative and differentiation capacity, may respond differently to mechanical stimuli and chemical signals, reflecting the different mechanisms involved in Ca^{2+} signal propagation. Whereas the anterior lens epithelium in general carries out active Ca^{2+} transport, the conceptual clearance scheme for circulating Ca^{2+} suggests that the equatorial epithelial cells are the primary site where the intracellular flux of Ca^{2+} is ultimately directed for active extrusion, thereby completing its circulation out of the lens.[10] Furthermore, previous work has shown that lens fiber cells respond robustly to stretch via AQP5 trafficking, whereas the epithelium exhibits no comparable redistribution of AQP1 or AQP5.[66] Thus, whereas stretching cannot be fully excluded as a source of perturbation in our preparation, its direct effects on the epithelial signaling studied here are likely minimal and comparable among different LC preparations.

Connexin-based gap junctions are central to Ca^{2+} handling in the lens and their conductance is tightly regulated by $[Ca^{2+}]_i$ through Ca^{2+}-calmodulin (CaM) feedback. This mechanism has been demonstrated in bovine[67] and ovine[16] lens epithelial primary cultures. Mutations in Cx46, predominantly expressed in lens fiber cells, can increase CaM binding affinity, reduce conductance, and alter sensitivity to both Ca^{2+} and pH.[68] Similarly, Cx43, the predominant connexin in LECs, contains a defined CaM-binding site.[69] Beyond regulation, connexins differ in permeability: Cx43 is permissive to IP_3 and cAMP, whereas Cx50 restricts their passage.[70] Cx43 also exhibits the highest, and Cx50 the lowest, permeability to cAMP.[71] In our model, junctions mediate IP_3 diffusion with short-range Ca^{2+} co-diffusion, consistent with these biophysical constraints. Connexin hemichannels, notably Cx43 and Cx46, are also expressed in the lens[72] and can contribute to mechanosensitive ATP release triggered by swelling or osmotic changes.[73] TRPV4 acts as an upstream regulator, with its activation increasing membrane conductance in LECs, consistent with hemichannel opening and ATP release,[74,75] whereas pannex-

Investigative Ophthalmology & Visual Science

ins have likewise been implicated.[76,77] PIEZO1 has also been investigated in the lens. In the mouse lens epithelium, its expression and mechanosensitive function have been demonstrated,[78] and activation of PIEZO1 was shown to modulate ion transport in the mouse lens.[79] Together, these findings suggest that PIEZO1 may represent an additional mechanosensory pathway in the human lens epithelium. These isoform-specific properties, regulatory mechanisms, and complementary release routes likely shape dynamic signaling architectures in the lens epithelium under stress, whereas the overall pattern of connexin expression remains conserved across mammals,[3] underscoring their physiological relevance.

Studies on other epithelial tissues provide insights into potential ATP-release mechanisms that might also apply to LECs. In renal epithelia, aldosterone can engage an autocrine/paracrine ATP signaling axis consistent with basolateral release[80] and ATP release has been observed across both apical and basolateral membranes in primary epithelial cultures.[81] In Xenopus A6 renal collecting-duct cell line, basolateral ATP has been linked to activation of $P2X_4$ receptors and modulation of ion-channel activity.[82] By analogy, it is plausible that LECs can release ATP from both membranes given their polarized nature, although direct evidence for basolateral release in LECs is still lacking. One limitation to note is that our experiments were conducted at room temperature rather than 37°C. Lower temperatures reduce metabolic activity and Ca^{2+}-ATPase kinetics, which can slow Ca^{2+} clearance compared with in vivo conditions. Although this may affect recovery dynamics, the main conclusions regarding intercellular signaling remain robust.

Our multicellular model builds on the theoretical framework of Vainio et al.[28] adapting their intracellular Ca^{2+} signaling module to human lens tissue and extending it with a more realistic representation of intercellular communication and epithelial geometry. Specifically, we replaced the simplified ring-layer topology with a tessellation-based geometry that captures heterogeneous cell-to-cell neighborhoods, incorporated explicit extracellular ATP turnover (allowing for non-regenerative, partially regenerative, and fully regenerative release), and constrained the framework using lens-specific pharmacological perturbations (CBX and apyrase). Whereas the model captures key features of epithelial Ca^{2+} wave propagation, it necessarily simplifies others: it omits Ca^{2+}-calmodulin feedback on connexins, isoform-specific permeability differences, and spatial heterogeneity in receptor expression, and it assumes uniform receptor density without dynamic mechanical deformation. Future refinements should therefore include ATP-gated P2X receptors, hemichannel- or pannexin-dependent ATP release kinetics, stretch-activated channels such as TRPV4 and PIEZO1, and store-operated Ca^{2+} entry, temperature effect, together with region-specific receptor and connexin distributions. Such additions would increase physiological realism, improve predictive capacity, and clarify how mechanical or metabolic stress perturbs intercellular communication in early cataract pathophysiology.

Taken together, our findings support a hybrid mechanism in which intercellular Ca^{2+} waves in the human lens epithelium emerge from a finely balanced interplay between gap-junctional diffusion and partially regenerative ATP-mediated paracrine signaling via P2Y receptors. Gap junctions enable rapid, localized Ca^{2+} signal transmission, principally through IP_3 (with short-range co-diffusion of Ca^{2+}), whereas extracellular ATP extends the spatial reach and duration of the response. Together with the perturbation experiments, the model indicates that neither passive ATP release nor gap-junctional diffusion alone can account for the observed spatiotemporal Ca^{2+}-wave patterns under our conditions. Because all recordings analyzed here derive from cataractous lenses, establishing whether the same coupling logic operates in non-cataractous human tissue (or suitable models) will require further study. More broadly, despite being non-excitable, the lens epithelium depends on spatially coordinated Ca^{2+} signaling to sustain ionic homeostasis and tissue transparency, functions that are vulnerable to aging, oxidative stress, and mechanical strain. As lens fiber cells lack robust active Ca^{2+} extrusion, efficient clearance of intracellular Ca^{2+} relies on intact epithelial function and intercellular communication. Disruption of these pathways, either through connexin dysfunction, altered ATP handling, or perturbed mechanotransduction, may contribute to early cataract pathophysiology. By integrating experiments with multicellular computational modeling, this work clarifies the complementary roles of junctional and paracrine routes and provides a framework for future investigations into how the lens signaling microenvironment maintains homeostasis, and how its dysregulation can initiate cataractogenesis.

Acknowledgments

Supported by the Slovenian Research and Innovation Agency (research core funding nos. P3-0333, P1-0055, P3-0396, and I0-0029, and research project nos. J3-60062 and J3-50107).

Disclosure: **M. Šterk**, None; **E. Thaler**, None; **A. Fajmut**, None; **M. Hawlina**, None; **M. Gosak**, None; **S. Andjelić**, None

References

1. Hogan MJ, Alvarado JA, Esperson Weddell J. *Histology of the human eye; an atlas and textbook*. Philadelphia, PA: Saunders; 1971.
2. Andjelic S, Drašlar K, Hvala A, Lopic N, Strancar J, Hawlina M. Anterior lens epithelial cells attachment to the basal lamina. *Acta Ophthalmol*. 2016;94(3):e183–e188.
3. Mathias RT, White TW, Gong X. Lens gap junctions in growth, differentiation, and homeostasis. *Physiol Rev*. 2010;90(1):179–206.
4. Sugiyama Y, Prescott AR, Tholozan FM, Ohno S, Quinlan RA. Expression and localisation of apical junctional complex proteins in lens epithelial cells. *Exp Eye Res*. 2008;87(1):64–70.
5. Dahm R, van Marle J, Quinlan RA, Prescott AR, Vrensen GF. Homeostasis in the vertebrate lens: mechanisms of solute exchange. *Philos Trans R Soc Lond B Biol Sci*. 2011;366(1568):1265–1277.
6. White TW. Unique and redundant connexin contributions to lens development. *Science (1979)*. 2002;295(5553):319–320.
7. Klein BEK, Klein R, Lee KE. Incidence of age-related cataract over a 10-year interval. *Ophthalmology*. 2002;109(11):2052–2057.
8. GBD 2019 Blindness and Vision Impairment Collaborators; Vision Loss Expert Group of the Global Burden of Disease Study. Causes of blindness and vision impairment in 2020 and trends over 30 years, and prevalence of avoidable blindness in relation to VISION 2020: the Right to Sight: an analysis for the Global Burden of Disease Study. *Lancet Glob Health*. 2021;9(2):e144–e160.
9. Duncan G, Williams MR, Riach RA. Calcium, cell signalling and cataract. *Prog Retin Eye Res*. 1994;13(2):623–652.

10. Gao J, Sun X, Martinez-Wittinghan FJ, Gong X, White TW, Mathias RT. Connections between connexins, calcium, and cataracts in the lens. *J Gen Physiol*. 2004;124(4):289–300.
11. Das GP, K J, Vasavada A. Causative and preventive action of calcium in cataracto-genesis. *Acta Pharmacol Sin*. 2004;25(10):1250–1256.
12. Rhodes JD, Sanderson J. The mechanisms of calcium homeostasis and signalling in the lens. *Exp Eye Res*. 2009;88(2):226–234.
13. Ohata H, Tanaka K, Maeyama N, Yamamoto M, Momose K. Visualization of elementary mechanosensitive Ca^{2+}-influx events, Ca^{2+} spots, in bovine lens epithelial cells. *J Physiol*. 2001;532(Pt 1):31–42.
14. Cooper KE, Tang JM, Rae JL, Eisenberg RS. A cation channel in frog lens epithelia responsive to pressure and calcium. *J Membr Biol*. 1986;93(3):259–269.
15. Rae JL, Mathias RT, Cooper K, Baldo G. Divalent cation effects on lens conductance and stretch-activated cation channels. *Exp Eye Res*. 1992;55(1):135–144.
16. Churchill GC, Lurtz MM, Louis CF. Ca(2+) regulation of gap junctional coupling in lens epithelial cells. *Am J Physiol Cell Physiol*. 2001;281(3):C972–C981.
17. Sanderson J, Dartt DA, Trinkaus-Randall V, et al. Purines in the eye: recent evidence for the physiological and pathological role of purines in the RPE, retinal neurons, astrocytes, Müller cells, lens, trabecular meshwork, cornea and lacrimal gland. *Exp Eye Res*. 2014;127:270–279.
18. DeRosa AM, Meşe G, Li L, et al. The cataract causing Cx50-S50P mutant inhibits Cx43 and intercellular communication in the lens epithelium. *Exp Cell Res*. 2009;315(6):1063–1075.
19. Rong P, Wang X, Niesman I, et al. Disruption of Gja8 (α8 connexin) in mice leads to microphthalmia associated with retardation of lens growth and lens fiber maturation. *Development*. 2002;129(1):167–174.
20. White TW, Bruzzone R. Intercellular communication in the eye: clarifying the need for connexin diversity. *Brain Res Rev*. 2000;32(1):130–137.
21. Collison DJ, Duncan G. Regional differences in functional receptor distribution and calcium mobilization in the intact human lens. *Invest Ophthalmol Vis Sci*. 2001;42(10):2355–2363.
22. Hu RG, Suzuki-Kerr H, Webb KF, et al. Molecular and functional mapping of regional differences in P2Y receptor expression in the rat lens. *Exp Eye Res*. 2008;87(2):137–146.
23. Suzuki-Kerr H, Lim JC, Donaldson PJ. Purinergic receptors in the rat lens: activation of P2X receptors following hyperosmotic stress. *Invest Opthalmol Vis Sci*. 2010;51(8):4156–4163.
24. Candia OA. Electrolyte and fluid transport across corneal, conjunctival and lens epithelia. *Exp Eye Res*. 2004;78(3):527–535.
25. Leybaert L, Sanderson MJ. Intercellular Ca^{2+} waves: mechanisms and function. *Physiol Rev*. 2012;92(3):1359–1392.
26. Gosak M, Markovič R, Fajmut A, Marhl M, Hawlina M, Andjelić S. The analysis of intracellular and intercellular calcium signaling in human anterior lens capsule epithelial cells with regard to different types and stages of the cataract. *PLoS One*. 2015;10(12):e0143781.
27. Gosak M, Gojić D, Spasovska E, Hawlina M, Andjelic S. Cataract progression associated with modifications in calcium signaling in human lens epithelia as studied by mechanical stimulation. *Life (Basel)*. 2021;11(5):369.
28. Vainio I, Abu Khamidakh A, Paci M, et al. Computational model of Ca^{2+} wave propagation in human retinal pigment epithelial ARPE-19 cells. *PLoS One*. 2015;10(6):e0128434.
29. Ceriani F, Pozzan T, Mammano F. Critical role of ATP-induced ATP release for Ca^{2+} signaling in nonsensory cell networks of the developing cochlea. *Proc Natl Acad Sci U S A*. 2016;113(46):E7194–E7201.
30. Warren NJ, Tawhai MH, Crampin EJ. Mathematical modelling of calcium wave propagation in mammalian airway epithelium: evidence for regenerative ATP release. *Exp Physiol*. 2010;95(1):232–249.
31. Brodskiy PA, Zartman JJ. Calcium as a signal integrator in developing epithelial tissues. *Phys Biol*. 2018;15(5):051001.
32. Konnerth A, Obaid AL, Salzberg BM. Optical recording of electrical activity from parallel fibres and other cell types in skate cerebellar slices in vitro. *J Physiol*. 1987;393(1):681–702.
33. Andjelić S, Zupančič G, Perovšek D, et al. Anterior lens capsule as a tool to study the physiology of human lens epithelial cells. *Zdravniški vestnik*. 2010;79:123–130.
34. Keizer J, Levine L. Ryanodine receptor adaptation and Ca^{2+}(-)induced Ca^{2+} release-dependent Ca^{2+} oscillations. *Biophys J*. 1996;71(6):3477–3487.
35. Bock M, Tyagi AK, Kreft JU, Alt W. Generalized voronoi tessellation as a model of two-dimensional cell tissue dynamics. *Bull Math Biol*. 2010;72(7):1696–1731.
36. Kaliman S, Jayachandran C, Rehfeldt F, Smith AS. Limits of applicability of the voronoi tessellation determined by centers of cell nuclei to epithelium morphology. *Front Physiol*. 2016;7:551.
37. Brown NAP, Bron AJ. An estimate of the human lens epithelial cell size in vivo. *Exp Eye Res*. 1987;44(6):899–906.
38. Kyoi T, Ueda F, Kimura K, Yamamoto M, Kateoka K. Development of gap junctions between gastric surface mucous cells during cell maturation in rats. *Gastroenterology*. 1992;102(6):1930–1935.
39. Hansen M, Boitano S, Dirksen ER, et al. Intercellular calcium signaling induced by extracellular adenosine 5′-triphosphate and mechanical stimulation in airway epithelial cells. *J Cell Sci*. 1993;106(4):995–1004.
40. Sanderson MJ, Charles AC, Dirksen ER. Mechanical stimulation and intercellular communication increases intracellular Ca^{2+} in epithelial cells. *Cell Regul*. 1990;1(8):585–596.
41. Potter GD, Byrd TA, Mugler A, Sun B. Communication shapes sensory response in multicellular networks. *Proc Natl Acad Sci USA*. 2016;113(37):10334–10339.
42. Schneidman E, Berry MJ, 2nd, Segev R, Bialek W. Weak pairwise correlations imply strongly correlated network states in a neural population. *Nature*. 2006;440(7087):1007–1012.
43. Stasiak SE, Jamieson RR, Bouffard J, Cram EJ, Parameswaran H. Intercellular communication controls agonist-induced calcium oscillations independently of gap junctions in smooth muscle cells. *Sci Adv*. 2020;6(32):eaba1149.
44. Weitz J, Menegaz D, Caicedo A. Deciphering the complex communication networks that orchestrate pancreatic islet function. *Diabetes*. 2021;70(1):17–26.
45. Azuma M, David LL, Shearer TR. Hydration and elevated calcium alone do not produce xylose nuclear cataract: role of proteolysis by calpain. *Ophthalmic Res*. 1992;24(1):8–14.
46. Churchill GC, Atkinson MM, Louis CF. Mechanical stimulation initiates cell-to-cell calcium signaling in ovine lens epithelial cells. *J Cell Sci*. 1996;109(2):355–365.
47. Fagerholm PP, Philipson BT. Human traumatic cataract. *Acta Ophthalmol*. 1979;57(1):20–32.
48. Donati V, Peres C, Nardin C, et al. Calcium signaling in the photodamaged skin: in vivo experiments and mathematical modeling. *Function*. 2021;3(1):aqzb064.
49. Handly LN, Wollman R. Wound-induced Ca^{2+} wave propagates through a simple release and diffusion mechanism. *Mol Biol Cell*. 2017;28(11):1457–1466.
50. Abu Khamidakh AE, Juuti-Uusitalo K, Larsson K, Skottman H, Hyttinen J. Intercellular Ca^{2+} wave propagation in human

Investigative Ophthalmology & Visual Science

retinal pigment epithelium cells induced by mechanical stimulation. *Exp Eye Res*. 2013;108:129–139.
51. Frame MK, de Feijter AW. Propagation of mechanically induced intercellular calcium waves via gap junctions and ATP receptors in rat liver epithelial cells. *Exp Cell Res*. 1997;230(2):197–207.
52. Isakson BE, Evans WH, Boitano S. Intercellular Ca^{2+} signaling in alveolar epithelial cells through gap junctions and by extracellular ATP. *Am J Physiol Lung Cell Mol Physiol*. 2001;280(2):L221–L228.
53. Kepseu WD, Woafo P. Long-range interaction effects on calcium-wave propagation. *Phys Rev E Stat Nonlin Soft Matter Phys*. 2008;78(1 Pt 1):011922.
54. Sneyd J, Wetton BT, Charles AC, Sanderson MJ. Intercellular calcium waves mediated by diffusion of inositol trisphosphate: a two-dimensional model. *Am J Physiol*. 19951;268(6 Pt 1):C1537–C1545.
55. Tabi CB, Kenne Tiayo T, Etémé AS, et al. Bifurcation of synchronized nonlinear intercellular Ca^{2+} oscillations induced by bi-directional paracrine signaling and inositol 1,4,5-triphosphate-cytosolic-Ca^{2+} interaction. *Phys Lett A*. 2024;498:129332.
56. Tiayo TK, Etémé AS, Tabi CB, Ekobena Fouda HP, Crépin Kofané T. Nonlinear dynamics of inositol 1,4,5-trisphosphate-induced Ca^{2+} patterns in two-dimensional cell networks with paracrine signaling interaction. *Nonlinear Dyn*. 2023;111(13):12593–12606.
57. Kobayashi Y, Sanno Y, Sakai A, et al. Mathematical modeling of calcium waves induced by mechanical stimulation in keratinocytes. *PLoS One*. 2014;9(3):e92650.
58. Bennett MR, Buljan V, Farnell L, et al. Purinergic junctional transmission and propagation of calcium waves in spinal cord astrocyte networks. *Biophys J*. 2006;91(9):3560–3571.
59. Goldberg M, De Pittà M, Volman V, Berry H, Ben-Jacob E. Nonlinear gap junctions enable long-distance propagation of pulsating calcium waves in astrocyte networks. *PLoS Comput Biol*. 2010;6(8):e1000909.
60. Höfer T, Venance L, Giaume C. Control and plasticity of intercellular calcium waves in astrocytes: a modeling approach. *J Neurosci*. 2002;22(12):4850–4859.
61. MacDonald CL, Yu D, Buibas M, Silva GA. Diffusion modeling of ATP signaling suggests a partially regenerative mechanism underlies astrocyte intercellular calcium waves. *Front Neuroeng*. 2008;1:1.
62. Kang M, Othmer HG. Spatiotemporal characteristics of calcium dynamics in astrocytes. *Chaos*. 2009;19(3):037116.
63. Edwards JR, Gibson WG. A model for Ca^{2+} waves in networks of glial cells incorporating both intercellular and extracellular communication pathways. *J Theor Biol*. 2010;263(1):45–58.
64. Michalski K, Kawate T. Carbenoxolone inhibits Pannexin1 channels through interactions in the first extracellular loop. *J Gen Physiol*. 2016;147(2):165–174.
65. Marian MJ, Mukhopadhyay P, Borchman D, et al. Plasma membrane Ca^{2+}-ATPase isoform expression in human cataractous lenses compared to age-matched clear lenses. *Ophthalmic Res*. 2008;40(2):86–93.
66. Petrova RS, Bavana N, Zhao R, Schey KL, Donaldson PJ. Changes to zonular tension alters the subcellular distribution of AQP5 in regions of influx and efflux of water in the rat lens. *Invest Opthalmol Vis Sci*. 2020;61(11):36.
67. Crow JM, Atkinson MM, Johnson RG. Micromolar levels of intracellular calcium reduce gap junctional permeability in lens cultures. *Invest Ophthalmol Vis Sci*. 1994;35(8):3332–3341.
68. Hu Z, Riquelme MA, Gu S, Jiang JX. Regulation of connexin gap junctions and hemichannels by calcium and calcium binding protein calmodulin. *Int J Mol Sci*. 2020;21(21):8194.
69. Zhou Y, Yang W, Lurtz MM, et al. Identification of the calmodulin binding domain of connexin 43. *J Biol Chem*. 2007;282(48):35005–35017.
70. Valiunas V, White TW. Connexin43 and connexin50 channels exhibit different permeability to the second messenger inositol triphosphate. *Sci Rep*. 2020;10(1):8744.
71. Brink PR, Valiunas V, White TW. Lens connexin channels show differential permeability to signaling molecules. *Int J Mol Sci*. 2020;21(18):6943.
72. Berthoud VM, Minogue PJ, Osmolak P, et al. Roles and regulation of lens epithelial cell connexins. *FEBS Lett*. 2014;588(8):1297–303.
73. Retamal MA, Altenberg GA. Role and posttranslational regulation of Cx46 hemichannels and gap junction channels in the eye lens. *Front Physiol*. 2022;13:864948.
74. Nakazawa Y, Petrova RS, Sugiyama Y, Nagai N, Tamura H, Donaldson PJ. Regulation of the membrane trafficking of the mechanosensitive ion channels TRPV1 and TRPV4 by zonular tension, osmotic stress and activators in the mouse lens. *Int J Mol Sci*. 2021;22(23):12658.
75. Ek-Vitorin JF, Shahidullah M, Delamere NA. Activation of transient receptor vanilloid 4 increases connexin hemichannel activity in porcine ciliary nonpigmented epithelium. *Front Biophys*. 2025;38:S1.
76. Suzuki-Kerr H, Walker KL, Han MH, Lim JC, Donaldson PJ. Hyposmotic stress causes ATP release in a discrete zone within the outer cortex of rat lens. *Mol Vis*. 2022;28:245–256.
77. Delamere NA, Mandal A, Shahidullah M. The significance of TRPV4 channels and hemichannels in the lens and ciliary epithelium. *J Ocul Pharmacol Ther*. 2016;32(8):504–508.
78. Allen A, Maddala R, Eldawy C, Rao PV. Mechanical load and Piezo1 channel regulated myosin II activity in mouse lenses. *Int J Mol Sci*. 2022;23(9):4710.
79. Shahidullah M, Rosales JL, Delamere N. Activation of Piezo1 increases Na,K-ATPase-mediated ion transport in mouse lens. *Int J Mol Sci*. 2022;23(21):12870.
80. Gorelik J, Zhang Y, Sánchez D, et al. Aldosterone acts via an ATP autocrine/paracrine system: the Edelman ATP hypothesis revisited. *Proc Natl Acad Sci USA*. 2005;102(42):15000–15005.
81. Wilson PD, Hovater JS, Casey CC, Fortenberry JA, Schwiebert EM. ATP release mechanisms in primary cultures of epithelia derived from the cysts of polycystic kidneys. *J Am Soc Nephrol*. 1999;10(2):218–229.
82. Zhang Y, Sanchez D, Gorelik J, et al. Basolateral $P2X_4$ -like receptors regulate the extracellular ATP-stimulated epithelial Na^+ channel activity in renal epithelia. *Am J Physiol Renal Physiol*. 2007;292(6):F1734–F1740.

Supplementary Material

Supplementary Video S1. Calcium activity in LECs following mechanical stimulation under control conditions, visualized as changes in the 360/380 nm fluorescence ratio. The ratio image series is superimposed on the 360 nm image to provide better morphological context. Green intensities correspond to elevated intracellular Ca^{2+} concentrations.
Supplementary Video S2. Calcium activity in LECs following mechanical stimulation under apyrase conditions, visualized as changes in the 360/380 nm fluorescence ratio. The ratio image series is superimposed on the 360 nm image to provide better

Investigative Ophthalmology & Visual Science

morphological context. Green intensities correspond to elevated intracellular Ca^{2+} concentrations.

Supplementary Video S3. Calcium activity in LECs following mechanical stimulation under CBX conditions, visualized as changes in the 360/380 nm fluorescence ratio. The ratio image series is superimposed on the 360 nm image to provide better morphological context. Green intensities correspond to elevated intracellular Ca^{2+} concentrations.

Supplementary Video S4. Simulated Ca^{2+} activity in a LEC network model for control conditions. Shades of green indicate Ca^{2+} concentration, with lighter shades representing low concentrations and darker shades representing high concentrations.

Supplementary Video S5. Simulated Ca^{2+} activity in a LEC network model for apyrase conditions. Shades of green indicate Ca^{2+} concentration, with lighter shades representing low concentrations and darker shades representing high concentrations.

Supplementary Video S6. Simulated Ca^{2+} activity in a LEC network model for CBX conditions. Shades of green indicate Ca^{2+} concentration, with lighter shades representing low concentrations and darker shades representing high concentrations.

Investigative Ophthalmology & Visual Science